

Continuum, cyclotron line, and absorption variability in the high-mass X-ray binary Vela X-1

C. M. Diez¹, V. Grinberg^{2,1}, F. Fürst³, E. Sokolova-Lapa^{4,5}, A. Santangelo¹, J. Wilms⁴, K. Pottschmidt^{6,7}, S. Martínez-Núñez⁸, C. Malacaria⁹, and P. Kretschmar¹⁰

¹ Institut für Astronomie und Astrophysik, Universität Tübingen, Sand 1, 72076 Tübingen, Germany
diez@astro.uni-tuebingen.de

² European Space Agency (ESA), European Space Research and Technology Centre (ESTEC), Keplerlaan 1, 2201 AZ Noordwijk, The Netherlands

³ Quasar Science Resources S.L for European Space Agency (ESA), European Space Astronomy Centre (ESAC), Camino Bajo del Castillo s/n, 28692 Villanueva de la Cañada, Madrid, Spain

⁴ Dr. Karl Remeis Sternwarte & Erlangen Centre for Astroparticle Physics, Friedrich-Alexander-Universität Erlangen-Nürnberg, Sternwartstr. 7, 96049 Bamberg, Germany

⁵ Sternberg Astronomical Institute, M. V. Lomonosov Moscow State University, Universitetskij pr., 13, Moscow 119992, Russia

⁶ CRESST, Department of Physics, and Center for Space Science and Technology, UMBC, Baltimore, MD 21250, USA

⁷ NASA Goddard Space Flight Center, Astrophysics Science Division, Greenbelt, MD 20771, USA

⁸ Instituto de Física de Cantabria (CSIC-Universidad de Cantabria), E-39005, Santander, Spain

⁹ Universities Space Research Association, Science and Technology Institute, 320 Sparkman Drive, Huntsville, AL 35805, USA

¹⁰ European Space Agency (ESA), European Space Astronomy Centre (ESAC), Camino Bajo del Castillo s/n, 28692 Villanueva de la Cañada, Madrid, Spain

Received 9 July 2021; accepted 23 December 2021

ABSTRACT

Because of its complex clumpy wind, prominent cyclotron resonant scattering features, intrinsic variability and convenient physical parameters (close distance, high inclination, small orbital separation) which facilitate the observation and analysis of the system, Vela X-1 is one of the key systems to understand accretion processes in high-mass X-ray binaries on all scales. We revisit Vela X-1 with two new observations taken with *NuSTAR* at orbital phases $\sim 0.68\text{--}0.78$ and $\sim 0.36\text{--}0.52$ which show a plethora of variability and allow us to study the accretion geometry and stellar wind properties of the system. We follow the evolution of spectral parameters down to the pulse period time-scale using a partially covered powerlaw continuum with a Fermi-Dirac cut-off to model the continuum and local absorption. We could confirm anti-correlations between the photon index and the luminosity and, for low fluxes, between the folding energy and the luminosity, implying a change of properties in the Comptonising plasma. We could not confirm a previously seen correlation between the cyclotron line energy and the luminosity of the source in the overall observation, but we observed a drop in the cyclotron line energy following a strong flare. We see strong variability in absorption between the two observations and within one observation (for the $\sim 0.36\text{--}0.52$ orbital phases) that can be explained by the presence of a large-scale structure, such as accretion- and photoionisation wakes in the system and our variable line of sight through this structure.

Key words. X-rays: binaries, stars: neutron, stars: winds, accretion

1. Introduction

Vela X-1 is an eclipsing high-mass X-ray binary (HMXB) consisting of a B0.5 Ib supergiant HD 77581 (Hiltner et al. 1972) and an accreting neutron star with a pulse period of ~ 283 s (McClintock et al. 1976) in a ~ 8.964 d orbit around the supergiant (Kreykenbohm et al. 2008). A thorough review of the Vela X-1 system is given by Kretschmar et al. (2021), who also discussed the role of this system in understanding HMXB systems in general. Here, we limit ourselves to points that are of immediate relevance for this work. The radius of HD 77581 is $30 R_{\odot}$ and the orbital separation $\sim 1.7 R_{\star}$ (van Kerkwijk et al. 1995; Quaintrell et al. 2003). The neutron star is thus embedded in the dense wind of the supergiant companion, which has a mass loss rate of $\sim 10^{-6} M_{\odot} \text{ yr}^{-1}$ (Watanabe et al. 2006). The source is located at $1.99^{+0.13}_{-0.11}$ kpc (Kretschmar et al. 2021) and is therefore one of the brightest persistent point sources in the X-ray sky despite a moderate mean luminosity of $5 \times 10^{36} \text{ erg s}^{-1}$ (Fürst et al. 2010).

The mass of the neutron star is estimated to be $\sim 1.7\text{--}2.1 M_{\odot}$ (Kretschmar et al. 2021).

The system is highly inclined ($>73^{\circ}$, van Kerkwijk et al. 1995) and thus facilitates the study of the accretion and wind physical properties through observations at different orbital phases (Haberl & White 1990; Goldstein et al. 2004; Watanabe et al. 2006; Fürst et al. 2010, e.g.). Doroshenko et al. (2013) showed a systematic change in the absorption along the orbit, when averaged among multiple orbits: in particular, average absorption decreased after the eclipse, reached a minimum at orbital phase of $\phi_{\text{orb}} \approx 0.3$ and grew afterwards, with a strong increase around $\phi_{\text{orb}} \approx 0.5$. However, measurements of absorption at same orbital phase are often different during different orbits of the system (Kretschmar et al. 2021). Fürst et al. (2010) also found deviations from a log-normal distribution in the histogram of the orbital phase averaged brightness distribution of Vela X-1 which could be due to the complex and turbulent accretion geometry of the system.

The overall large-scale wind structure in Vela X-1 has been investigated in different publications over the years. [Odaka et al. \(2013\)](#) interpreted the observed strong changes in absorption of Vela X-1 on short time-scales with *Suzaku* due to the compact object's motion in the supersonic stellar wind forming a bow shock. [Eadie et al. \(1975\)](#) suggested an accretion wake in Vela X-1 based on the absorption dips that showed up in the lightcurve of the *Ariel V* Sky Survey Experiment. Accretion and photoionisation wakes and possibly tidal stream have also been raised (see e.g. [Nagase et al. 1983](#); [Sato et al. 1986](#); [Blondin et al. 1990](#); [Kaper et al. 1994](#); [van Loon et al. 2001](#); [Malacaria et al. 2016](#)).

An accretion wake forms through the focussing of the stellar wind by the influence of the gravitational field of the neutron star, leading to an unsteady bow shock in the vicinity of the neutron star ([Blondin et al. 1991](#); [Manousakis & Walter 2015](#); [Malacaria et al. 2016](#)).

A photoionisation wake is formed when the wind interacts with the Strömgren sphere, created around the neutron star because of photoionisation of the wind material

(see figure 2 in [Watanabe et al. 2006](#)). Hydrodynamical simulations optimised for Vela X-1 have been conducted in [Blondin et al. \(1990\)](#) and [Manousakis \(2011\)](#) where they showed the formation of the wakes and overall a complex large-scale structure in the wind. [Grinberg et al. \(2017\)](#) illustrated the accretion and photoionisation wakes in the Vela X-1 system in their figure 1 based on the simulations published in [Manousakis \(2011\)](#).

Even beyond the variable absorption, Vela X-1 is known to be an intrinsically highly variable source and has shown bright flares ([Martínez-Núñez et al. 2014](#); [Kreykenbohm et al. 2008](#); [Lomaeva et al. 2020](#)) and off-states ([Kreykenbohm et al. 2008](#); [Doroshenko et al. 2011](#)) where the observed flux decreased to less than 10% of its normal value ([Kreykenbohm et al. 2008](#); [Sidoli et al. 2015](#)).

The off-states have been interpreted in the context of a highly structured wind of the companion by some authors ([Kreykenbohm et al. 2008](#); [Ducci et al. 2009](#); [Fürst et al. 2010](#)), while for instance in the models of [Manousakis & Walter \(2015\)](#), hydrodynamic instabilities are sufficient to explain the origin of the off-states without the need of intrinsic inhomogeneities in the stellar wind. Another theory to explain the origin of the off-states in Vela X-1 is the interaction of the neutron star's magnetosphere with the plasma ([Doroshenko et al. 2011](#)).

Beyond the off-states, variations in the mass accretion rate leading to the observed flares and the variable absorption require, at least to some degree, a clumpy structure of the wind ([Kreykenbohm et al. 2008](#); [Fürst et al. 2010](#); [Martínez-Núñez et al. 2014](#)).

Vela X-1 shows various features in its X-ray spectrum, typical for accreting neutron stars. Around 6.4 keV, a prominent fluorescent emission line associated with FeK α , first reported in [Becker et al. \(1978\)](#). Some previous analyses with high resolution instruments (e.g. [Watanabe et al. 2006](#)) have also detected FeK β while others, at different orbital phases, struggled to constrain this feature ([Amato et al. 2021](#)). [Watanabe et al. \(2006\)](#) stated there are three possible origins to the presence of those lines in Vela X-1: the extended stellar wind, reflection off the stellar photosphere and the accretion wake. Another observed line-like feature in the spectrum of X-ray pulsars is the so-called 10 keV feature. The physical origin of this feature is still unknown ([Coburn et al. 2002](#)) and may be caused by our incomplete understanding of the continuum spectrum and usually modeled with simple phenomenological models. It appears to be an inherent feature in the spectra of accreting pulsars ([Coburn et al. 2002](#)) and probably reflects the limitations of the simple phe-

nomenological models used ([Staubert et al. 2019](#)). It may appear in emission in some sources, such as 4U 0115+63 ([Ferrigno et al. 2009](#); [Müller et al. 2013](#)) and EXO 2030+375 ([Klochkov et al. 2007](#)). It is then modelled with a broad Gaussian emission component and is often referred to as the '10 keV bump' model ([Reig & Nespoli 2013](#)). In other sources, it has been found in absorption, such as in XTE J0658–073 ([McBride et al. 2006](#); [Nespoli et al. 2012](#)), in Cen X-3 ([Santangelo et al. 1998](#)), or in Vela X-1 ([Fürst et al. 2014b](#)) and modeled with a broad Gaussian absorption component ([Fürst et al. 2014b](#)). In 4U 1901+03 ([Reig & Milonaki 2016](#)) and KS 1947+300 ([Fürst et al. 2014a](#)) similar features have been interpreted as of possible magnetic origin.

Cyclotron resonant scattering features (CRSF, or cyclotron lines) appear as broad absorption lines in the X-ray spectra of highly magnetised neutron stars whose magnetic field strength can be then directly measured from the CRSF energy. The fundamental CRSF is the result of resonant scattering of photons by electrons in strong magnetic fields from the ground level to the first excited Landau level followed by radiative decay (see [Staubert et al. 2019](#), for a review and references therein). At higher excited Landau levels, the resulting cyclotron lines are called harmonics. The spectrum of Vela X-1 has been confirmed to show two cyclotron lines ([Kreykenbohm et al. 2002](#)): a prominent harmonic line at ~ 55 keV and a weaker fundamental at ~ 25 keV ([Kendziorra et al. 1992](#); [Kretschmar et al. 1997](#); [Orlandini et al. 1998](#); [Kreykenbohm et al. 1999, 2002](#); [Fürst et al. 2014b](#)). In Vela X-1, the harmonic line is broader and deeper than the fundamental line, which can be so weak that it cannot be significantly detected in some observations ([Odaka et al. 2013](#)). The study of the CRSF energy variability with luminosity is important to determine physical properties of the source (see Sect. 6.1.2).

In several accreting X-ray pulsars it was observed that the correlation of the cyclotron line energy with the luminosity and the correlation of the photon index with luminosity were inverse to each other, that is if one was positive, the other was negative (e.g. [Klochkov et al. 2011](#), for a sample study). There are theoretical expectations for a correlation between the CRSF energy and luminosity.

Following [Becker et al. \(2012\)](#), the variation of the CRSF energy with luminosity is due to the variation of the emission height within the accretion column that characterises the line-forming region. They define a source as being in the supercritical accretion regime when the radiation field has a dynamic effect on the infalling plasma. In this regime, the accretion flow is decelerated in the extended radiative shock, the height of which increases with the mass-accretion rate. It can move the line forming region away from the surface of the neutron star, to the higher altitudes corresponding to the lower magnetic field; however, not necessarily up to the shock height (see e.g. [Nishimura 2014](#)). This can explain the negative correlation of the cyclotron line centroid energy with luminosity. The alternative model is suggested by [Poutanen et al. \(2013\)](#) based on the reflection of the radiation from the neutron star surface at different altitudes. The so-called critical luminosity L_{crit} is associated with the transition from the negative correlation of the cyclotron line energy and luminosity, to the positive one. It is understood that in sub-critical regime (the X-ray luminosity $L_X < L_{\text{crit}}$) the role of the radiation in the stopping of the accretion flow becomes negligible. There are several mechanisms proposed for the matter deceleration in the sub-critical regime, that can explain the observed positive correlation of the cyclotron line energy with the luminosity. The matter can be decelerated to the rest by Coulomb collisions in the accretion channel. The height at which the effective stopping

occurs decreases with the increasing luminosity (Staubert et al. 2007; Becker et al. 2012), causing the positive correlation. Another scenario Mushtukov et al. (2015b), suggests that the shift of the cyclotron line energy to the lower values with the decreasing luminosity can be also explained by the Doppler effect in the accretion channel moderated by the luminosity-dependent velocity profile. The other possibility at low mass-accretion rates is the origination of the collisionless shock above the surface (Langer & Rappaport 1982). The height of this shock decreases with increasing mass accretion rate (Shapiro & Salpeter 1975), thus moving the line-forming region closer to the surface of the neutron star and resulting in the positive correlation of the cyclotron line energy and luminosity (Rothschild et al. 2017; Vybornov et al. 2017).

The value L_{crit} corresponding to the transition between the subcritical and supercritical regimes is dependent on the magnetic field of the source and the geometry of the accretion channel. The analytical expressions were obtained, for example by Basko & Sunyaev (1976) and Becker et al. (2012), under different considerations. The critical luminosity is calculated numerically as a function of the magnetic field of the neutron star, for different geometries types of accretion on the (disc- and wind-accretion) by Mushtukov et al. (2015a), taking into account the resonance in the Compton scattering cross sections and the possible mixture of polarisation modes. It was shown, that the critical luminosity is not a monotonic function of the magnetic field strength.

For Vela X-1, a tentative detection of such a correlation between cyclotron line energy and luminosity has been presented in Fürst et al. (2014b). For Vela X-1, it was also found (e.g. Odaka et al. 2013; Fürst et al. 2014b) that Γ was anti-correlated with the luminosity, indicating that this source was in a subcritical accretion regime, behaving similarly to sources such as Her X-1 (Staubert et al. 2007) and GX 304-1 (Yamamoto et al. 2011).

Given the importance of Vela X-1 for the study of wind-accreting neutron stars, we use two further observations with *NuSTAR*, taken at different orbital phases of the source, to map the accretion environment and the structure of the stellar wind in the source and to further investigate possible correlations of the CRSF with other spectral parameters. First, we describe the two datasets and the analysis software used in Sect. 2. We then present the lightcurves and timing results of those observations in Sect. 3. We proceed to a time-averaged spectroscopy in Sect. 4 and to a time-resolved spectroscopy in Sect. 5. We discuss the results in Sect. 6, focussing on the wind structure and the CRSFs, and give a summary and an outlook in Sect. 7.

2. Observation and data reduction

NuSTAR (Harrison et al. 2013) observed Vela X-1 on 10–11 January 2019 and on 3–5 May 2019 as science target using the two Focal Plane Modules A and B (FPMA and FPMB). We then have two datasets with an exposure of ~ 36 ks and ~ 40 ks, referred as observation I and observation II respectively. Details about the observations are given in Table 1 and Fig. 1 shows the count rate of the Vela X-1 system against the orbital phase. As can be seen from Fig. 1, observation II consists of two parts. The interruption is due to data loss caused by problems with the ground station and the corresponding data cannot be recovered. This sketch also includes the *Swift*/BAT 15–50 keV lightcurve averaged over all data since 2005 and therefore representing the averaged behaviour of the source smoothing out the variability

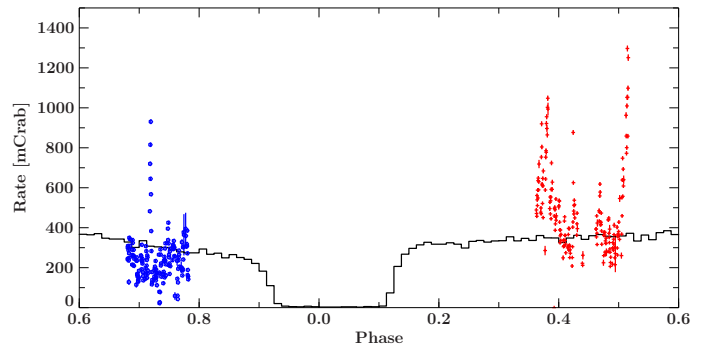


Fig. 1: *NuSTAR* 3–79 keV flux for observation I (blue) on January 2019 and observation II on May 2019 (red) with a time resolution of $P_I = 283.4532$ sec and $P_{II} = 283.4447$ sec respectively and *Swift*/BAT 15–50 keV flux averaged over all data since 2005 (black solid line) plotted over the neutron star's orbital phase where $\phi_{\text{orb}} = 0$ is defined with T_{90} .

on shorter time-scales (Fürst et al. 2010; Kretschmar et al. 2021). The eclipse is clearly visible around $\phi_{\text{orb}} = 0$.

The orbital phases ϕ_{orb} are derived from the ephemeris from Kreykenbohm et al. (2008) and Bildsten et al. (1997), see Table 2. Several definitions of the time of phase zero can be found in the literature. The most common are T_{ecl} and T_{90} . T_{ecl} is the mid-eclipse time whereas T_{90} is the time when the mean longitude l is equal to 90° . For the particular case of Vela X-1, those two points are very close to each other, the difference is of the order of $\Delta\phi \approx 0.02$. Nonetheless, in soft X-rays the eclipse boundaries can be hard to define and considering that the orbit is elliptical, defining T_{ecl} is not always that clean. Explanations on how to convert T_{90} to T_{ecl} can be found in Kreykenbohm et al. (2008). In this work, we exclusively use T_{90} .

The two observations are carried out at different orbital phases. At the orbital phase of observation I that is at $\phi_{\text{orb}} \approx 0.75$, the accretion and photoionisation wakes are placed along the line of sight of the observer, see figure 1 in Grinberg et al. (2017). Thus, a different behaviour of the absorption is expected compared to observation II at $\phi_{\text{orb}} \approx 0.4$ – 0.5 , where the wakes may be starting to pass through the observer's line of sight.

We use the NUSTARDAS pipeline v2.0.0 and HEASOFT v6.28 with *NuSTAR* CALDB (calibration database) v20200826 applied with the clock correction to extract spectra and lightcurves for the time-averaged observations and we also proceed to extract spectra orbit-by-orbit and pulse-by-pulse, necessary for a time-resolved analysis of this highly variable source (see Sect. 5). For the orbit-by-orbit spectroscopy, we extract a spectrum for each *NuSTAR* orbit around the Earth. That leads to 14 spectra for observation I and 19 spectra for observation II. For the pulse-by-pulse spectroscopy, we extract a spectrum for each rotation of the neutron star, with the corresponding integration pulse period derived for this observation (see Sect. 3). That leads to 168 spectra for observation I and 209 spectra for observation II. The event times are barycentred using the *barycorr* tool from NUSTARDAS pipeline and corrected for the binary orbit using the ephemeris from Table 2. We use the Interactive Spectral Interpretation System (ISIS) v1.6.2-47 (Houck & Denicola 2000) to analyse the data and note that ISIS allows access to XSPEC (Arnaud 1996) models that are referenced later in the text.

We extract source spectra from a region with ~ 82 arcsec radius for observation I and ~ 67 arcsec radius for observation II around Vela X-1's FK5 coordinates, separately for FPMA and

Table 1: Observation details.

Name	Obs ID	Time Start MJD (day) binarycor	Time Stop MJD (day) binarycor	Exposure (ks)	Orbital phase (with T_{90})	Orbital phase (with T_{ec1})
Obs I	90402339002	58493.1813	58494.0910	36.086	0.68–0.78	0.65–0.75
Obs II	30501003002	58606.8688	58608.2465	40.562	0.36–0.52	0.34–0.49
<i>Obs IIa</i>	<i>30501003002</i>	<i>58606.8688</i>	<i>58607.5660</i>	<i>22.557</i>	<i>0.36–0.44</i>	<i>0.34–0.42</i>
<i>Obs IIb</i>	<i>30501003002</i>	<i>58607.7625</i>	<i>58608.2465</i>	<i>18.005</i>	<i>0.46–0.52</i>	<i>0.44–0.49</i>

As observation II is divided into two parts, observation IIa and IIb for the analysis, we list the details for both sub-observations above.

Table 2: Ephemeris used.

Reference	Orbital parameter	Value	Units
Kreykenbohm et al. (2008)	Time of mean longitude equal to $\pi/2$ (T_{90})	52974.001 ± 0.012	MJD (day)
Kreykenbohm et al. (2008)	Mid-eclipse time (T_{ec1})	52974.227 ± 0.007	MJD (day)
Kreykenbohm et al. (2008)	Orbital period (P_{orb})	8.964357 ± 0.000029	day
Bildsten et al. (1997)	Semimajor axis ($a \sin i$)	113.89 ± 0.13	lt-sec
Bildsten et al. (1997)	Eccentricity (e)	0.0898 ± 0.0012	
Bildsten et al. (1997)	Longitude of periastron (ω)	152.59 ± 0.92	
van Kerkwijk et al. (1995)	Inclination (i)	> 73	$^{\circ}$

FPMB. As Vela X-1 is very bright, it illuminates the whole focal plane, and we thus extract background spectra circular regions with ~ 63 arcsec radius for observation I and ~ 67 arcsec radius for observation II as far away from the source as possible for both observations to minimise source influence on background estimation. Since the background changes over the field-of-view of the instrument, systematic uncertainties are formally introduced by this method. Vela X-1, however, is about a factor 5 brighter than the background even at the highest energies used here, such that the effect of residual uncertainties is negligible.

Due to a thermal blanket tear, the detector focal plane module FPMA requires a low energy effective area correction ([Madsen et al. 2020](#)). Such a correction is automatically applied in all NuSTAR CALDB releases starting with the 20200429 CALDB. However, for some sources the automatic procedure results in an over-correction. This is the case for our observation II, where the automatic procedure results in stark differences between the focal plane modules. After consulting with the NuSTAR calibration team (K. Madsen, priv. comm), the best approach was decided to be to revert to the old FPMA ARF¹ for this observation which results in an agreement between the modules.

All spectra are rebinned within ISIS to a minimal signal to noise of 5 adding at least 2, 3, 5, 8, 16, 18, 48, 72 and 48 channels for energies between 3.0–10, 10–15, 15–20, 20–35, 35–45, 45–55, 55–65, 65–76 and 76–79 keV, respectively. Uncertainties are given at the 90% confidence ($\Delta\chi^2 = 2.7$ for one parameter of interest), unless otherwise noted.

3. Lightcurves and timing

3.1. Pulse period

The pulse period of Vela X-1 shows strong variations on all time-scales mainly due to a highly variable accretion rate. It varies in a way mostly consistent with random-walk ([de Kool &](#)

[Anzer 1993](#)). To measure this period accurately to do the pulse-by-pulse analysis in Sect. 5, we perform epoch-folding ([Leahy 1987](#)) on the FPMA extracted lightcurve with 1 sec binning. A pulse period of $P_{\text{I}} = 283.4532 \pm 0.0008$ sec for observation I and of $P_{\text{II}} = 283.4447 \pm 0.0004$ sec for observation II are found, which is consistent with the overall pulse period history of Vela X-1 from *Fermi* GBM². The pulse period changes by such a small fraction ($\pm \sim 0.06\%$ at most) within one observation that it is not enough to induce significant shifts in the pulse phase in the pulse-by-pulse analysis. The uncertainties are estimated using a Monte Carlo simulation ([Larsen & Monakhov 1996](#)) with 2000 runs.

3.2. Lightcurves

Vela X-1 is known to be a highly variable source, thus we present the lightcurves of observations I and II in the top panels of Fig. 2 to investigate the relevant features. We bin the lightcurves to the spin period of the neutron star to avoid the intra-pulse variability.

In observation I, at $T_{\text{obs}} \approx 58493.53$ MJD, we can observe a large flare indicated in the left upper panel of Fig. 2 where the source flux increases to ~ 200 counts s^{-1} per module, from an average of ~ 60 counts s^{-1} during the whole observation. Moreover, two off-states are detected at $T_{\text{obs}} \approx 58493.66$ MJD and $T_{\text{obs}} \approx 58493.93$ MJD. Here, the source flux drops to ~ 6 –7 counts s^{-1} for the first off-state and ~ 10 counts s^{-1} for the second one.

In observation II, the average source flux is ~ 118 counts s^{-1} about twice as much as during observation I. At $T_{\text{obs}} \approx 58606.95$ MJD, $T_{\text{obs}} \approx 58607.03$ MJD, $T_{\text{obs}} \approx 58607.42$ MJD and $T_{\text{obs}} \approx 58608.23$ MJD four major flares indicated in the right upper panel of Fig. 2 are detected reaching ~ 220 counts s^{-1} , ~ 275 counts s^{-1} , ~ 228 counts s^{-1} and ~ 238 counts s^{-1} respectively. However, this time no off-state is detected. The big gap in observation II between $T_{\text{obs}} \approx 58607.57$ MJD and $T_{\text{obs}} \approx 58607.76$ MJD is due to the loss of data.

¹https://nustarsoc.caltech.edu/NuSTAR_Public/NuSTAROperationSite/mli.php

²<https://gamma-ray.nsstc.nasa.gov/gbm/science/pulsars/lightcurves/velax1.html>

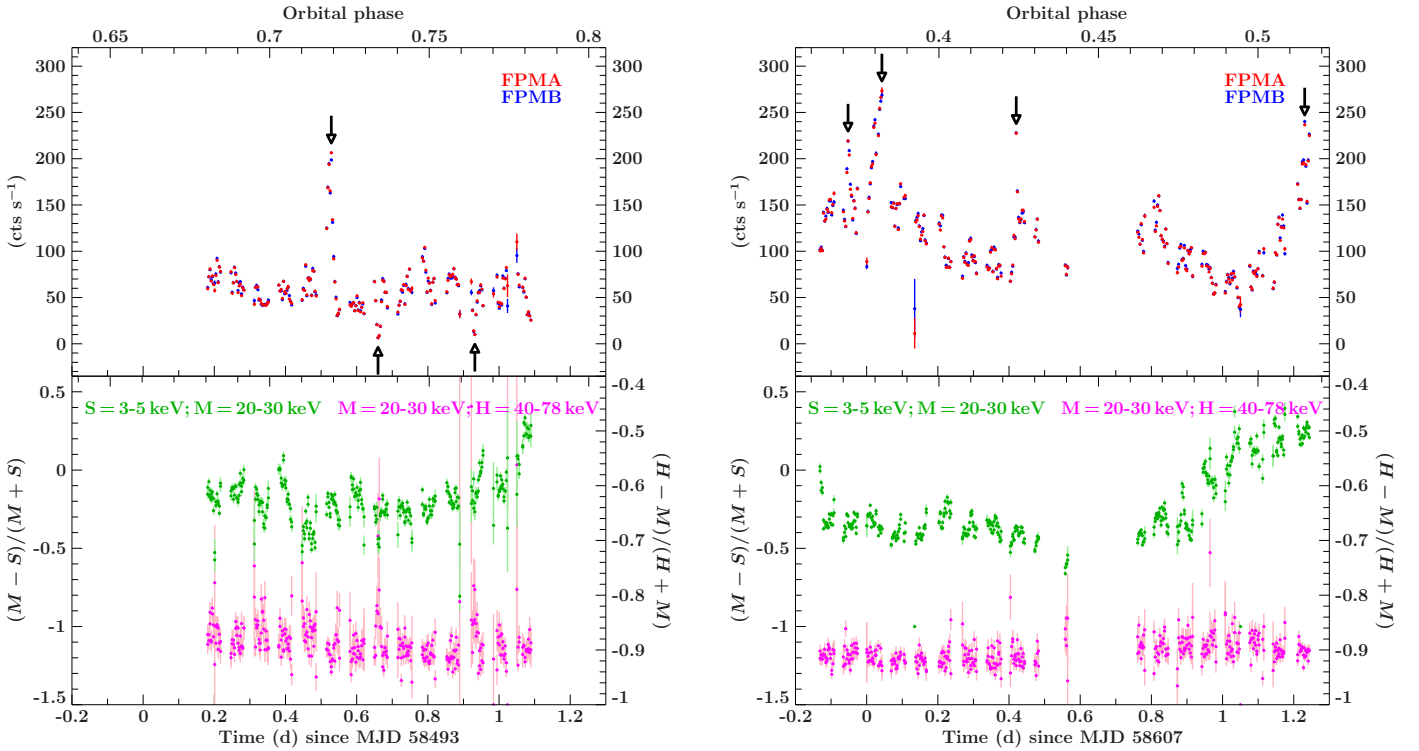


Fig. 2: Lightcurves and hardness ratios for observations I (left panel) and II (right panel) with a time resolution of $P_I = 283.4532$ sec and $P_{II} = 283.4447$ sec respectively. Major off-states and major flares are indicated by arrows. Green points show the hardness ratio between the 3–5 keV and the 20–30 keV bands using the left-hand y-axis. Magenta points show the hardness ratio between the 20–30 keV and the 40–78 keV bands using the right-hand y-axis.

3.3. Hardness ratios

In the bottom panels of Fig. 2, we present the hardness ratios calculated as $HR = (\text{Medium} - \text{Soft})/(\text{Medium} + \text{Soft})$ (left-hand y-axis) and $HR = (\text{Hard} - \text{Medium})/(\text{Hard} + \text{Medium})$ (right-hand y-axis) with three different energy bands. The low-energy ratio (in green) covers the energy region where most of the absorption from the stellar wind happens and thus, we will try to compare it to the high-energy ratio (in magenta) which is less impacted by the effect of the stellar wind absorption and instead more representative of the true underlying continuum shape.

In observation II, we observe that the 3–5 keV to 20–30 keV hardness behaves differently before and after the data loss period: it is roughly constant before and rising after, while the 20–30 keV to 40–78 keV hardness shows no such trends. This motivates us to divide observation II into two parts to be analysed separately: observation IIa and observation IIb which correspond to the data before and after the loss respectively (details can be found in Table 1). Moreover, the time-averaged modelling of the spectrum of observation II leads to a bad description of the data, supporting the choice of a separate analysis (see Sect. 4).

In observation I, there are two changes at $T_{\text{obs}} \approx 58493.67$ MJD and $T_{\text{obs}} \approx 58493.92$ MJD which correspond to the location of the two off-states. However, there is no change associated with the flare in any of both hardness ratios. This has already been observed in the flares analysed in Kreykenbohm et al. (2008) or Fürst et al. (2014b). The spectrum becomes slightly harder in the low-energy ratio towards the end of the observation, but the hardness shows no other strong overall trends.

In observation II, the high-energy hardness ratio shows the exact same behaviour than during observation I. However, this time we do not see any strong change as no off-state was ob-

served during this observation. Again, no significant change in both hardness ratios is shown at the location of the flares. The spectrum in the low-energy ratio remains roughly flat for the first part of the observation but becomes suddenly harder starting from $T_{\text{obs}} \approx 58607.75$ MJD, which corresponds to the end of the period where the data were lost.

The changes in the hardness ratios observed during the off-states and the time variability of Vela X-1 during observations I and II require a spectral analysis of the source on shorter time-scales. To achieve this goal, we start by analysing the spectra averaged over the three effective observations (Obs I, Obs IIa and Obs IIb) as a basis for the further analysis (Sect. 4). We then continue analysing the orbit-by-orbit spectra to have a first overview of the evolution of various spectral parameters over time and use these values as inputs for the pulse-by-pulse spectroscopy. Both analyses are detailed in Sect. 5. This step-by-step time-resolved spectral analysis allows us to have a fine adjustment of the parameters and a follow-up of the parameters along the time at each step of the analysis. Finally, the obtained results are discussed in Sect. 6.

4. Time-averaged spectroscopy

4.1. Choice of continuum model

We first address the choice of the overall continuum model. Different flavours of powerlaw models with high energy cut-offs are used in the literature to empirically describe the continuum spectral shape of accreting neutron stars (e.g. Staubert et al. 2019).

The Fermi-Dirac cut-off (FDcut; Tanaka 1986) is the most widely used continuum model for Vela X-1, see Kreykenbohm et al. (1999, 2008); Fürst et al. (2014b). Thus, we use a powerlaw

with the photon index Γ and FDCut with the cut-off energy E_{cut} and the folding energy E_{fold} so that:

$$F(E) \propto E^{-\Gamma} \times \left(1 + \exp\left(\frac{E - E_{\text{cut}}}{E_{\text{fold}}}\right)\right)^{-1} \quad (1)$$

In this model, we constrain E_{fold} and E_{cut} to 4–18 keV and 18–40 keV, respectively to avoid model degeneracies. With this model, we are able to achieve a good description of the data, see Sect. 4.2 for an in depth discussion.

We also investigate several other models to fit all our observations. The same trends have been observed for all of them but for simplicity, we are only quoting below the values for observation I. The best-fit parameters for the time-averaged tested models can be found in the Appendix (Tables A.1 and A.2).

We attempt to describe the data with a `highecut`³ model, another often used model for the continuum in accreting neutron stars (Santangelo et al. 1998; Staubert et al. 2019). It results in a statistically worse description of the data than the FDCut model.

We also used the NPEX (Mihara 1995) model for the continuum which consists of a sum of a negative and a positive powerlaw which is then modified by an exponential cutoff that is characterised by a folding energy. This model has been previously used for a number of HMXBs (see, e.g. Hemphill et al. 2014; Jaisawal & Naik 2016). We explore the NPEX with the 10 keV feature (see following Sect. 4.2 for a more detailed discussion about the modelling of the 10 keV feature) parameter space. The combination of two powerlaws with wide allowed ranges of indices makes the analysis difficult and provides several combinations of good fits. If the positive powerlaw is fixed to 2, the function is known to be a good approximation of the unsaturated Comptonisation spectrum in neutron stars (Makishima et al. 1999; Odaka et al. 2013; Hemphill et al. 2014). This results in a good fit ($\chi^2/\text{dof} \approx 604.15/456$), with both powerlaw components of NPEX contributing to the continuum, but both cyclotron lines are very broad and deep (see following Sect. 4.2 for a more detailed discussion about the modelling of the CRSFs), in particular the strength of the harmonic cyclotron line reaches 83 ± 10 , effectively altering the continuum. Moreover, the norm of the positive powerlaw index was found close to 0, approaching a single powerlaw with a high energy cut-off. While statistically satisfactory, this model is thus not a good description of the data (see, e.g. Bissinger né Kühnel et al. 2020, for discussion of similar problems for a different HMXB). We also explore the NPEX without the 10 keV feature parameter space but it also results in a bad description of the continuum modelled by a too deep harmonic cyclotron line.

We further explore a Comptonisation continuum, using a single `compTT` (Titarchuk 1994) in a spherical accretion case as done previously in Maitra & Paul (2013) for Vela X-1. This results in a statistically good description of the data for both with and without 10 keV feature cases, but the overly strong cyclotron lines again effectively alter the continuum. A double `compTT` model has been recently proposed for several X-ray pulsars (see, e.g. Doroshenko et al. 2012; Tsygankov et al. 2019), albeit for the low luminosity regime below Vela X-1's luminosity. We also explore this double `compTT` model without the 10 keV feature, as it should in theory get rid of the absorption feature observed in the 10 keV range. We obtain a good fit (χ^2/dof is 622.53/456, slightly larger but similar to the FDCut best-fit) where the parameters can be constrained and the CRSFs behave as expected (if

both T_0 are tied and allowed to vary up to 1 keV, otherwise if they are free to vary in a wider range of values then the CRSFs become very strong again), showing around the same values as our FDCut best-fit model. However, the behaviour of the Comptonisation components does not agree with expectations from previous applications of this model and defies previous physical interpretation. Tsygankov et al. (2019), who introduced this model for the low luminosity state of GX 304-1, discuss that the components are likely to be independent. In particular, the low-energy component ($kT \lesssim 2$ keV) can be explained as radiation from hotspots at the neutron star's surface heated up by the accretion process. However, in our analysis, this component is much hotter, with $kT \approx 6.9$ keV. Additionally, in the low luminosity case, the two Comptonisation continua are of equal strength, while in our model the hotter component dominates the overall flux and spectral shape.

Overall, we conclude that the FDCut model offers the best empirical description of the continuum that we can obtain. Since it also allows us direct comparison with previous results, especially Fürst et al. (2014b) because different continua may lead to shifts in derived CRSF positions (e.g. Müller et al. 2013), we decide to adopt it for further modelling.

4.2. Modelling

We introduce a floating cross-normalisation parameter C_{FPMB} in order to give the relative normalisation between *NuSTAR*'s two detectors: FPMA and FPMB.

We try modelling the fluorescent emission lines features associated with $\text{FeK}\alpha$ and $\text{FeK}\beta$ with narrow Gaussian components. The $\text{FeK}\beta$ line cannot be constrained because of the limited energy resolution of *NuSTAR* and the overlapping Fe K-edge at 7.1 keV. Thus we only include the $\text{FeK}\alpha$ line around 6.4 keV in our final model.

For our analysis, we model the CRSFs using two multiplicative Gaussian absorption lines (`gabs` in XSPEC³) corresponding to the fundamental CRSF,F and to the harmonic CRSF,H with:

$$\text{CRSF}(E) = \exp\left[-\left(\frac{d}{\sigma\sqrt{2\pi}}\right)\exp\left(-0.5\left(\frac{E - E_{\text{cyc}}}{\sigma}\right)^2\right)\right] \quad (2)$$

d is the line depth and σ the line width.

We describe the 10 keV feature with a broad Gaussian line in absorption, as also done in Fürst et al. (2014b). We first try to describe the spectrum without this feature. However, the analysis leads to visible residuals in absorption in the 10 keV region for observation IIa and a bad description of the overall continuum which is compensated by deeper and broader CRSFs that effectively alter the continuum for all observations. We therefore conclude that the feature is necessary for a good description of our data. The physical origin of this 10 keV feature is unclear. The 10 keV feature in absorption has been found in other sources (McBride et al. 2006; Nespoli et al. 2012; Santangelo et al. 1998) and only sometimes tentatively associated with a cyclotron line (Reig & Milonaki 2016; Fürst et al. 2014a). In Vela X-1, it has so far never been interpreted as a cyclotron resonant scattering feature, although we cannot definitely exclude such an origin currently.

We further have to constrain the width of the fundamental line, setting it ad hoc to $\sigma_{\text{CRSF,F}} = 0.5 \times \sigma_{\text{CRSF,H}}$, following previous work (Fürst et al. 2014b). This value is based on the fact that the width of the CRSF is dominated by thermal broadening, for which σ/E is independent of energy (Schwartz et al. 2017). As $E_{\text{CRSF,F}}/E_{\text{CRSF,H}}$ is roughly 0.5, we use 0.5 for the

³<https://heasarc.gsfc.nasa.gov/xanadu/xspec/manual/node129.html>

width ratio as well. Letting the width free results in too wide fundamental CRSF that effectively describes the continuum in the 10–30 keV range. We do, however, verify, that when the line width is free, the best-fit cyclotron line energies, especially for the harmonic line, do not change significantly. Further, freezing the line width to a slightly larger value does not change the resulting best fit significantly. However, much narrower fundamental line (0.2 of the harmonic) leads to an increase of the reduced chi-square ($\chi^2/\text{dof} \approx 716.96/456$ for observation I) explained by a too narrow fundamental line shifting down the line energy of ~ 1 keV.

To describe the different absorption components surrounding the neutron star, we use the `tbabs` model (Wilms et al. 2000) and the corresponding abundances and cross-sections (Verner et al. 1996). We first try a single-absorption model but the spectrum is not well described at low energies, as can be seen on the example of observation I (Fig. 4 c). This can be understood as a high contribution of the absorption from the stellar wind at low energies. Therefore, we use a partial covering model with the covering fraction CF to take into account the clumpy structure of the stellar wind. The allowed values for CF range between 0 and 1. Different set ups of a partial covering model or equivalent models have previously been shown to be necessary to describe the spectrum of Vela X-1 well (e.g. Martínez-Núñez et al. 2014; Fürst et al. 2014b; Malacaria et al. 2016).

Therefore, our final and best-fit model can be written as:

$$I(E) = (CF \times N_{H,1} + (1 - CF)) \times N_{H,2} \times (F(E) \times \text{CRSF}, F \times \text{CRSF}, H + \text{FeK}\alpha + 10 \text{ keV}) \quad (3)$$

This partial covering model is equivalent to the partial covering model used in Fürst et al. (2014b) in order to allow easier comparison of the spectral parameters. The only difference lies in the description of the absorption components (see Fig. 3) that are differently parametrised between the two models. In Fürst et al. (2014b), they split the absorption component into two absorption columns: one corresponding to the absorption from the interstellar medium and the other one corresponding to both the absorption from the interstellar medium and from the stellar wind. In this work, we used two distinct absorption columns to describe the stellar wind and the absorption from the interstellar medium in order to have access to both parameters separately.

The absorption $N_{H,1}$ corresponding to the stellar wind embedding the neutron star is free and the absorption from the interstellar medium $N_{H,2}$ has been fixed to $3.71 \times 10^{21} \text{ cm}^{-2}$ based on NASA's HEASARC N_H tool website⁴ (HI4PI Collaboration et al. 2016). We also tested to leave $N_{H,2}$ as free parameter of the fit. For observation I, we obtain a high upper limit, consistent with the fixed value. For both parts of observation II, we obtain higher values that also lead to a systematic decrease in the photon index Γ . Given that *NuSTAR* does not cover the range below 3 keV, it is challenging to constrain low values of $N_{H,2}$, especially for a partial coverer. We thus decide to fix the $N_{H,2}$ to the theoretical galactic column density value for the following analysis.

We first show the contribution from the broad line components in Figs. 4 and 5. We observe a broad, strong contribution of the harmonic CRSF at around 54 keV and a much weaker fundamental CRSF at ~ 25 keV (residual panel b), as commonly found for this source (Kreykenbohm et al. 2002; Fürst et al. 2014b). There is also a visible contribution of the 10 keV feature (residual panel c).

The best-fit parameters for the three observations are presented in Table 3. There is an increase in the stellar wind absorption $N_{H,1}$ between observations IIa and IIb together with an increase in the covering fraction CF. Even though the energy of the fundamental cyclotron line $E_{\text{CRSF},F}$ remains almost constant, we can notice variability in the energy of the harmonic cyclotron line $E_{\text{CRSF},H}$ between the three observations. The folding energy E_{fold} remains constant within the uncertainties between the three observations whereas we can observe a variable cut-off energy E_{cut} . The unabsorbed flux $\mathcal{F}_{3-79 \text{ keV}}$ is higher by a factor of 2 in observations IIa and IIb than in observation I, following the higher count rates observed. The comparatively poor fit in observation IIa is driven by the low energies, where the spectrum appears even more complex than the model assumes (Fig. 5).

5. Time-resolved spectroscopy

Now that we have a good description of the average continuum of Vela X-1 for our observations, we can use the model to access the variability of the source on shorter time-scales. The good sensitivity of *NuSTAR* enables us to extract a spectrum for each *NuSTAR* orbit and also for each rotation of the neutron star. However, an analysis on a shorter time-scale than the pulse period is not expedient because the spectrum is highly variable with the pulse phase (see Kreykenbohm et al. 2002; La Barbera et al. 2003; Maitra & Paul 2013).

We use the model in Eq. 3 for the time-resolved spectroscopy using the same parameter ranges that we have used for the time-averaged spectroscopy. However, given the shorter exposure time per spectrum and consequently lower signal-to-noise ratio, we have to fix some more parameters (see Table 3) to their time-averaged values to obtain meaningful constraints on our model parameters. As the background is stable during the observation, we use the time-averaged background for all of the sliced-data since it provides a better estimate of the true background spectrum due to the higher signal-to-noise.

Due to its proximity to and thus degeneracy with $E_{\text{CRSF},F}$, the E_{cut} parameter has to be fixed for the orbit-by-orbit analysis. We further fix the line widths of both harmonic and fundamental CRSFs, $\sigma_{\text{CRSF},H}$ and $\sigma_{\text{CRSF},F}$, the line width of the FeK α line, $\sigma_{\text{FeK}\alpha}$, the energy of the 10 keV feature, $E_{10 \text{ keV}}$, the line width of the 10 keV feature, $\sigma_{10 \text{ keV}}$, and the floating cross-normalisation parameter, C_{FPMB} , to their respective time-averaged values.

For the pulse-by-pulse spectroscopy, we start with the same settings and fixed parameters as for the orbit-by-orbit spectroscopy. However, several of the remaining parameters are not well constrained by these data. Thus, we have to fix the strengths $d_{\text{CRSF},H}$ and $d_{\text{CRSF},F}$ and energies $E_{\text{CRSF},H}$ and $E_{\text{CRSF},F}$ of both harmonic and fundamental CRSFs to their respective orbit-wise values.

We show the results of both orbit-by-orbit and pulse-by-pulse spectral analyses as functions of time and orbital phase for observations I and II (IIa–IIb) in Figs. 6 and 7 respectively.

Some of the individual values presented correspond to observations with very short exposures and can be usually recognised as outliers with large uncertainties. This is in particular the case for orbit-wise spectra at orbits number 10, 11 and 12. These data have been affected by the loss of data due to ground station problems. Several pulse-wise outliers are located at the edges of the individual orbits where the data covers only a part of a given pulse. When discussing possible parameter correlations, these measurements have to be treated with caution. The off-states can be clearly seen in our data, but are too short for a detailed spectral analysis.

⁴<https://heasarc.gsfc.nasa.gov/cgi-bin/Tools/w3nh/w3nh.pl>

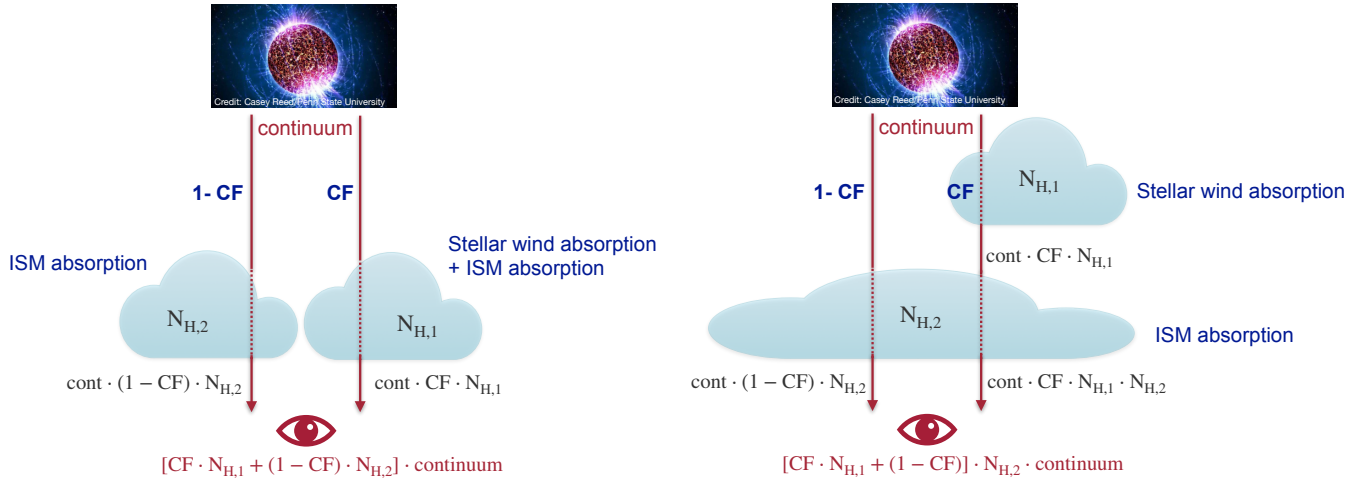


Fig. 3: Comparison of the partial covering model from Fürst et al. (2014b) (left side) and the partial covering model from this work (right side). The continuum corresponds to $(F(E) \times CRSF, F \times CRSF, H + FeK\alpha + 10 \text{ keV})$ in both cases.

Table 3: Best-fit parameters for the time-averaged final model.

Parameter	Obs I	Obs IIa	Obs IIb	Orbit-by-orbit	Pulse-by-pulse
C_{FPM}	1	1	1	1	1
C_{FPMB}	1.0203 ± 0.0021	1.0142 ± 0.0018	1.0204 ± 0.0022	\Rightarrow fixed	\Rightarrow fixed
$N_{H,1} (10^{22} \text{ cm}^{-2})$	34.0 ± 1.0	32.1 ± 1.9	$42.8^{+1.2}_{-1.3}$	fitted	fitted
$N_{H,2} (10^{22} \text{ cm}^{-2})$	fixed to 0.371	fixed to 0.371	fixed to 0.371	fixed to 0.371	fixed to 0.371
Γ	1.09 ± 0.05	$1.084^{+0.024}_{-0.025}$	$1.01^{+0.04}_{-0.05}$	fitted	fitted
$E_{cut} (\text{keV})$	$19.9^{+3.5}_{-2.0}$	$26.1^{+1.1}_{-1.2}$	21 ± 4	\Rightarrow fixed	\Rightarrow fixed
$E_{fold} (\text{keV})$	$12.6^{+0.9}_{-0.8}$	$10.2^{+0.5}_{-0.4}$	$11.2^{+1.1}_{-2.1}$	fitted	fitted
$E_{CRSF,F} (\text{keV})$	$24.7^{+1.0}_{-0.9}$	$24.3^{+1.0}_{-1.1}$	$24.0^{+0.0}_{-0.8}$	fitted	\Rightarrow fixed
$\sigma_{CRSF,F} (\text{keV})$	fixed to $0.5 \times \sigma_{CRSF,H}$	fixed to $0.5 \times \sigma_{CRSF,H}$	fixed to $0.5 \times \sigma_{CRSF,H}$	\Rightarrow fixed	\Rightarrow fixed
$d_{CRSF,F} (\text{keV})$	$0.75^{+0.00}_{-0.19}$	$0.31^{+0.16}_{-0.11}$	$0.86^{+0.00}_{-0.24}$	fitted	\Rightarrow fixed
$E_{CRSF,H} (\text{keV})$	$53.8^{+1.1}_{-0.9}$	51.8 ± 0.7	$56.0^{+2.0}_{-1.2}$	fitted	\Rightarrow fixed
$\sigma_{CRSF,H} (\text{keV})$	$7.9^{+1.3}_{-0.9}$	$7.4^{+0.8}_{-0.6}$	$8.8^{+6.6}_{-1.2}$	\Rightarrow fixed	\Rightarrow fixed
$d_{CRSF,H} (\text{keV})$	18^{+6}_{-4}	$16.5^{+3.1}_{-2.5}$	$18.58^{+0.00}_{-4.65}$	fitted	\Rightarrow fixed
$E_{FeK\alpha} (\text{keV})$	6.364 ± 0.012	6.357 ± 0.006	6.356 ± 0.008	fitted	fitted
$A_{FeK\alpha} (\text{ph s}^{-1} \text{ cm}^{-2})$	$(1.35 \pm 0.11) \times 10^{-3}$	$(4.04^{+0.17}_{-0.16}) \times 10^{-3}$	$(4.50^{+0.23}_{-0.22}) \times 10^{-3}$	fitted	fitted
$\sigma_{FeK\alpha} (\text{keV})$	$0.070^{+0.029}_{-0.045}$	$0.045^{+0.023}_{-0.045}$	$0.074^{+0.021}_{-0.025}$	\Rightarrow fixed	\Rightarrow fixed
$E_{10 \text{ keV}} (\text{keV})$	$9.5^{+0.6}_{-1.0}$	$9.13^{+0.14}_{-0.17}$	$9.2^{+0.5}_{-0.6}$	\Rightarrow fixed	\Rightarrow fixed
$A_{10 \text{ keV}} (\text{ph s}^{-1} \text{ cm}^{-2})$	$(-4.8^{+2.2}_{-4.8}) \times 10^{-3}$	$-0.0125^{+0.0017}_{-0.0023}$	$(-4.5^{+1.6}_{-2.4}) \times 10^{-3}$	fitted	fitted
$\sigma_{10 \text{ keV}} (\text{keV})$	$3.2^{+1.0}_{-0.7}$	$2.34^{+0.22}_{-0.18}$	$2.1^{+0.6}_{-0.5}$	\Rightarrow fixed	\Rightarrow fixed
$\mathcal{F}_{3-79 \text{ keV}} (\text{keV s}^{-1} \text{ cm}^{-2})$	$3.43^{+0.10}_{-0.05}$	$6.35^{+0.09}_{-0.00}$	$6.24^{+2.89}_{-0.10}$	fitted	fitted
$\mathcal{F}_{3-79 \text{ keV}} (\text{erg s}^{-1} \text{ cm}^{-2})$	$(5.49^{+0.17}_{-0.08}) \times 10^{-9}$	$(10.2^{+0.1}_{-0.00}) \times 10^{-9}$	$(10.0^{+4.4}_{-0.4}) \times 10^{-9}$	fitted	fitted
CF	0.883 ± 0.005	$0.505^{+0.012}_{-0.013}$	0.852 ± 0.005	fitted	fitted
χ^2/dof	613.37/456	731.94/456	578.30/456		

In the two right-most columns, we indicate which spectral parameters are fixed to the value found in the corresponding analysis at lower time resolution or still left free during the fit.

A significant variability of the presented parameters with time and orbital phase is observed in observations I and II. In particular, during the flare in observation I (at $T_{\text{obs}} \approx 58493.53 \text{ MJD}$), Γ reaches its minimal value while the energy of the $FeK\alpha$, which is rather stable otherwise, increases.

Significant variations of the energy of cyclotron lines and especially $E_{CRSF,H}$ can be observed in both datasets for the orbit-by-orbit spectral analysis. In observation IIb the values of $E_{CRSF,H}$ are higher than during observation IIa. In observation I, $E_{CRSF,H}$ is at higher energies before than after the flare. The fundamental line is much weaker than the harmonic and thus the

uncertainties on the values are much larger, preventing us from drawing conclusions on any correlations.

The stellar wind absorption is high in both observations. $N_{H,1}$ in observation I averages around $\sim 40 \times 10^{22} \text{ cm}^{-2}$. In observation II, it is more variable, in particular during observation IIb, it shows a rapid increase to more than $\sim 50 \times 10^{22} \text{ cm}^{-2}$.

The covering fraction CF remains stable around 0.9 for observation I. In observation II, CF is more variable, ranging between ~ 0.3 and ~ 1 and is higher during observation IIb than during observation IIa. During flares, the covering fraction tends to decrease on the pulse-by-pulse time-scale as visible in ob-

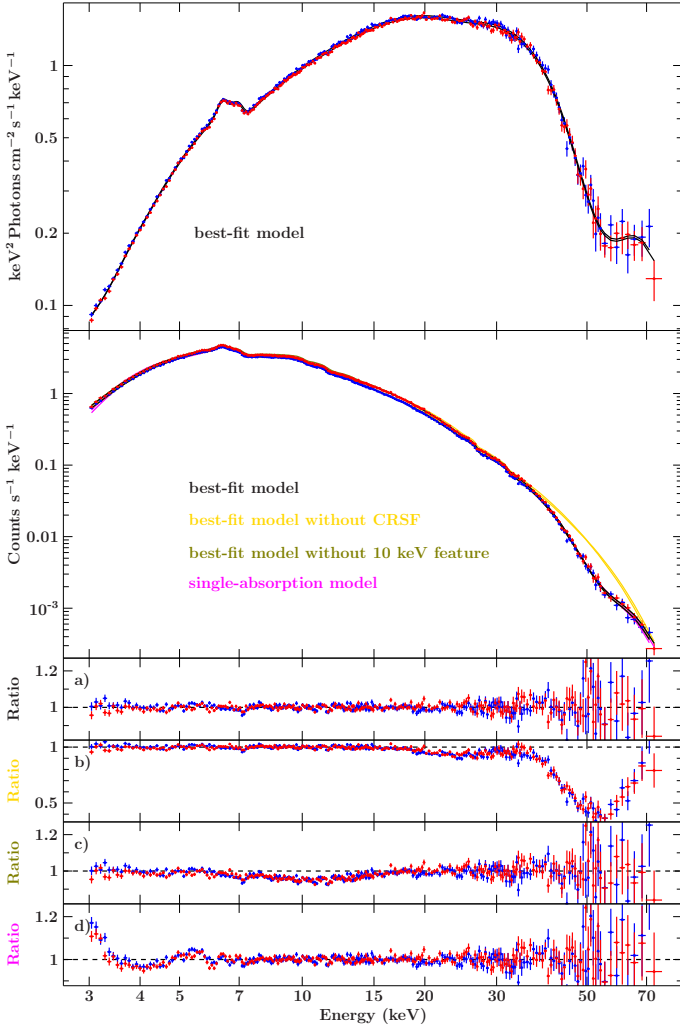


Fig. 4: Time-averaged spectrum for observation I. FPMA data in red and FPMB data in blue, models for both focal plane modules are shown in the same colour and are hardly distinguishable with the naked eye. The first two panels show respectively the unfolded spectrum and the count spectrum. Top-down description of the residual panels: a) best-fit model (black), b) best-fit model with CRSFs (yellow) turned off but not fitted again, c) best-fit model with 10 keV feature (green) turned off but not fitted again, d) single-absorption model (magenta). Green and magenta lines almost hidden by data and best-fit model in the data panel

servation I at $T_{\text{obs}} \approx 58493.53$ MJD or in observation II at $T_{\text{obs}} \approx 58606.95$ MJD, at $T_{\text{obs}} \approx 58607.03$ MJD and at $T_{\text{obs}} \approx 58607.42$ MJD. During off-states ($T_{\text{obs}} \approx 58493.66$ MJD and at $T_{\text{obs}} \approx 58493.93$ MJD in observation I), which corresponds to a minimum in $\mathcal{F}_{3-79 \text{ keV}}$, the CF tends to reach its maximal value of 1.

The folding energy E_{fold} seems to show distinct behaviour during both the flare and the off-states, but a correlation cannot be easily concluded without further investigation (see Sect. 6).

6. Discussion

6.1. Spectral shape and CRSF variability with luminosity

In this subsection, to compare our results to previous work and to other sources, we have to convert our observed 3–79 keV flux,

$\mathcal{F}_{3-79 \text{ keV}}$, to the 3–79 keV luminosity, $L_{3-79 \text{ keV}}$, using $\mathcal{F}_{3-79 \text{ keV}} = L_{3-79 \text{ keV}} / (4\pi d^2)$ where d is the distance to the source and is equal to $1.99^{+0.13}_{-0.11}$ kpc (Kretschmar et al. 2021). Overall, our luminosities are in the range of $\sim 2\text{--}10 \times 10^{36} \text{ erg s}^{-1}$ (Fig. 8) and thus slightly but not drastically below the often quoted range of around or a few $10^{37} \text{ erg s}^{-1}$ for the critical luminosity (e.g. Reig & Nespoli 2013). Uncertainties on the distance lead to systematic uncertainties in the overall luminosity of the source of approximately +15%/-12%. For this work, we chose to use an empirical model to describe the spectrum of Vela X-1 in order to get insights into the underlying physics which will be discussed below.

6.1.1. Continuum spectral shape

In the upper panel of Fig. 8, we show our results for the correlation between Γ and the luminosity. We also include previous measurements by Fürst et al. (2014b) at orbital phase 0.655–0.773, re-scaled to the updated distance to the source. We can observe a negative correlation between the spectral slope and the luminosity. This behaviour is typical for a source in the sub-critical accretion regime as it has already been found for example for Her X-1 (Staubert et al. 2007), Vela X-1 (Odaka et al. 2013; Fürst et al. 2014b), and several Be/X-ray pulsars in the sub-critical accretion regime (Reig & Nespoli 2013). Assuming X-ray radiation dominated by Comptonisation, this correlation can be a consequence of the increase of the accretion rate resulting in an increase of the X-ray luminosity and to a more efficient Comptonisation occurring in the accreted plasma (Odaka et al. 2013).

On Fig. 9, we can also see an anti-correlation between E_{fold} and luminosity as already indicated in Figs. 6 and 7 for lower luminosities ($\lesssim 4 \times 10^{36} \text{ erg s}^{-1}$). For higher luminosities, the folding energy seems to be constant around ~ 10 keV. Considering the underlying shape of the model we employ, we expect a positive degeneracy between the folding energy E_{fold} and the X-ray flux (or luminosity). Confidence maps calculated for folding energy and flux indeed confirm this expectation, implying that the observed opposite trend cannot be explained by modelling degeneracies. Odaka et al. (2013) use a different continuum model (NPEX) when analysing *Suzaku* data, so that the values of their and our parameters called folding energy cannot be directly compared. The trends, however, are comparable: they also find a negative correlation followed by a stabilisation between folding energy and flux at higher fluxes. Similar behaviour of the cut-off has been observed in a sample of Be/X-ray binaries when modelling their spectra with a cut-off powerlaw in the sub-critical accretion regime (Reig & Nespoli 2013). Assuming a significant contribution of not only bulk, but also thermal Comptonisation to the overall emission (Becker & Wolff 2007; Ferrigno et al. 2009), the change in the cut-off would correspond to a change in the temperature of the Comptonising plasma.

6.1.2. Accretion regime

To verify the accretion regime of Vela X-1 for our observations, we compute its critical luminosity using the equation 32 from Becker et al. (2012):

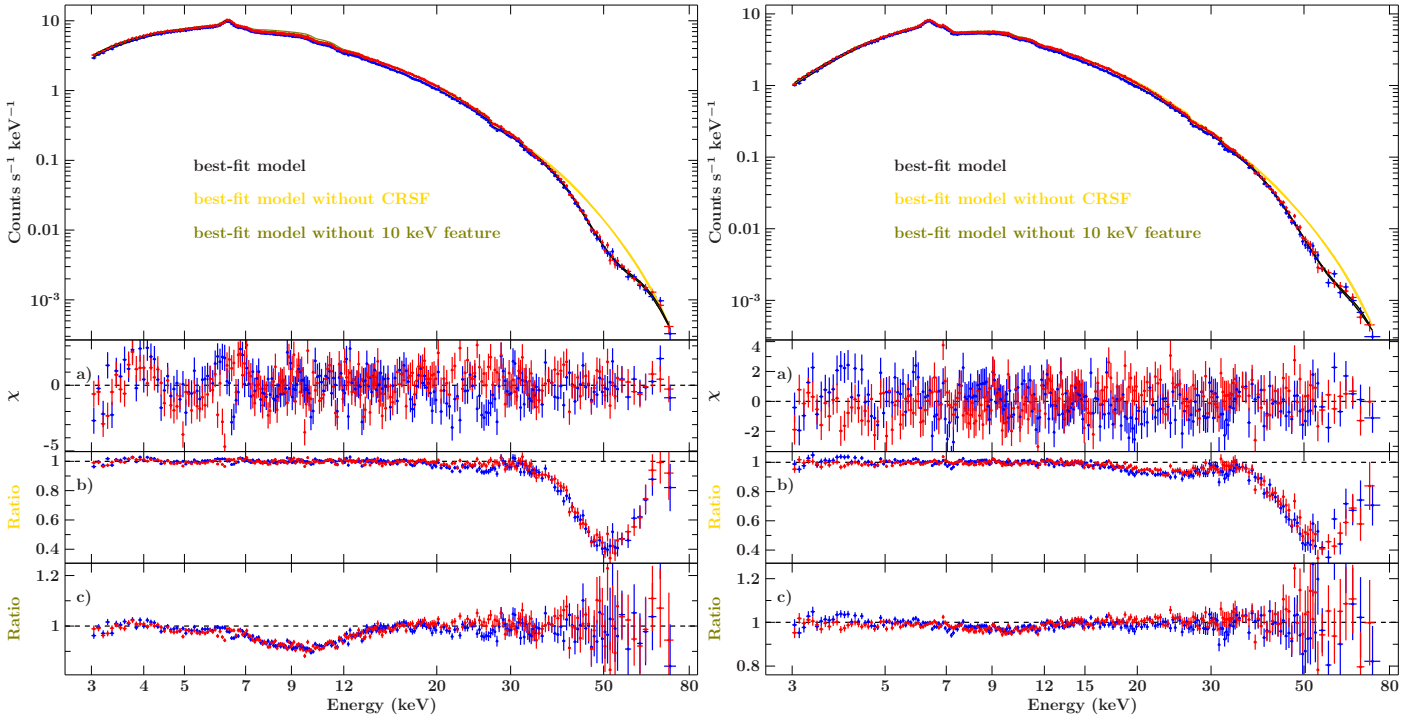


Fig. 5: Time-averaged spectrum for observation IIa (left panel) and IIb (right panel). FPMA data in red and FPMB data in blue, models for both focal plane modules are shown in the same colour and are hardly distinguishable with the naked eye. Top-down description of the residual panels: a) best-fit model (black), b) best-fit model with CRSFs (yellow) turned off but not fitted again, c) best-fit model with 10 keV feature (green, line almost hidden by data and best-fit model in the data panel) turned off but not fitted again.

$$L_{\text{crit}} = 1.49 \times 10^{37} \text{ erg s}^{-1} \left(\frac{\Lambda}{0.1} \right)^{-7/5} \omega^{-28/15} \times \left(\frac{M_{\text{NS}}}{1.4 M_{\odot}} \right)^{29/30} \left(\frac{R_{\text{NS}}}{10 \text{ km}} \right)^{1/10} \left(\frac{E_{\text{NS},n}}{n \times 11.57 \text{ keV}} \right)^{16/15} \quad (4)$$

where M_{NS} and R_{NS} are the mass and radius of the neutron star and ω is a parameter describing the spectral shape inside the column. $E_{\text{NS},n}$ is the surface cyclotron fundamental ($n = 1$) or harmonic ($n = 2$) energy of the neutron star. We use $\omega = 1$ (assuming that the spectrum inside the emission region is dominated by Bremsstrahlung). Recent publications (Legred et al. 2021) tend to assume a typical neutron star radius R_{NS} around 12 km. However, for this work, we use $R_{\text{NS}} = 10$ km under the same assumptions as in Becker et al. (2012) for typical neutron star parameters⁵. We consider a mass of $\sim 1.7\text{--}2.1 M_{\odot}$ (Kretschmar et al. 2021) and a surface fundamental cyclotron energy of $E_{\text{NS}} = 20$ keV.

Parameter Λ in Eq. 4 accounts for the difference in location of the Alfvén surface in case of the predominantly orbital or radial inflow (see, for example, equation 18 from Lamb et al. 1973). It depends on the ratio of the radial velocity of the flow to the free-fall one and on the thickness of the accretion disc. However, the Alfvén radius is reduced only by a factor of ~ 10 ($\Lambda \sim 0.1$) from the radius corresponding to a fully radial inflow even for the extreme values of these parameters (small radial velocities and a thin accretion disc). For spherical accretion, $\Lambda = 1$ and for disc accretion $\Lambda < 1$ (Becker et al. 2012). In the

case of Vela X-1, we consider a wind accreting source so the accretion is more likely to be spherical than through an accretion disc, although there are theoretical predictions of possible disc formation (El Mellah et al. 2019) and observational hints that temporarily a disc can be formed sometimes (Liao et al. 2020). Additionally, even without the presence of a disc, the accretion from the clumpy, disturbed wind of the companion is more complex than a simple spherical accretion case (e.g. El Mellah et al. 2018).

If we consider a spherical accretion with $\Lambda = 1$, then $L_{\text{crit}} \approx 0.13\text{--}0.15 \times 10^{37} \text{ erg s}^{-1}$ using Eq. 4, taking into account uncertainties on the mass, which classifies Vela X-1 as a super-critical source. However, in previous works, Vela X-1 has been classified as a sub-critical source (Fürst et al. 2014b) assuming $\Lambda = 0.1$ (thus disc accretion case), also following Becker et al. (2012). Indeed, for $\Lambda = 0.1$, we obtain $L_{\text{crit}} \approx 3.22\text{--}3.95 \times 10^{37} \text{ erg s}^{-1}$. Our assumption of $E_{\text{NS}} = 20$ keV is conservative. Given that the measured energy of the fundamental line is above 20 keV, the real value is likely higher and will lead to a higher L_{crit} . For instance, assuming $E_{\text{NS}} = 30$ keV, we obtain a $L_{\text{crit}} \approx 4.97\text{--}6.10 \times 10^{37} \text{ erg s}^{-1}$. This approach puts Vela X-1 in the sub-critical regime which would also be supported by the observed anti-correlation between Γ and luminosity (see Fig. 8) typical for a sub-critical source (Staubert et al. 2007; Odaka et al. 2013; Reig & Nespola 2013; Fürst et al. 2014b). However, the choice of $\Lambda = 0.1$ assumes a disc accretion case which we question for our observations.

A further theoretical calculation for the critical luminosity has been presented in Mushtukov et al. (2015a), taking into account the exact Compton scattering cross-section in the high magnetic field and in particular they show the results of their cal-

⁵The critical luminosity with a neutron star radius of 12 km is $\sim 2\%$ higher than the critical luminosity using a neutron star radius of 10 km.

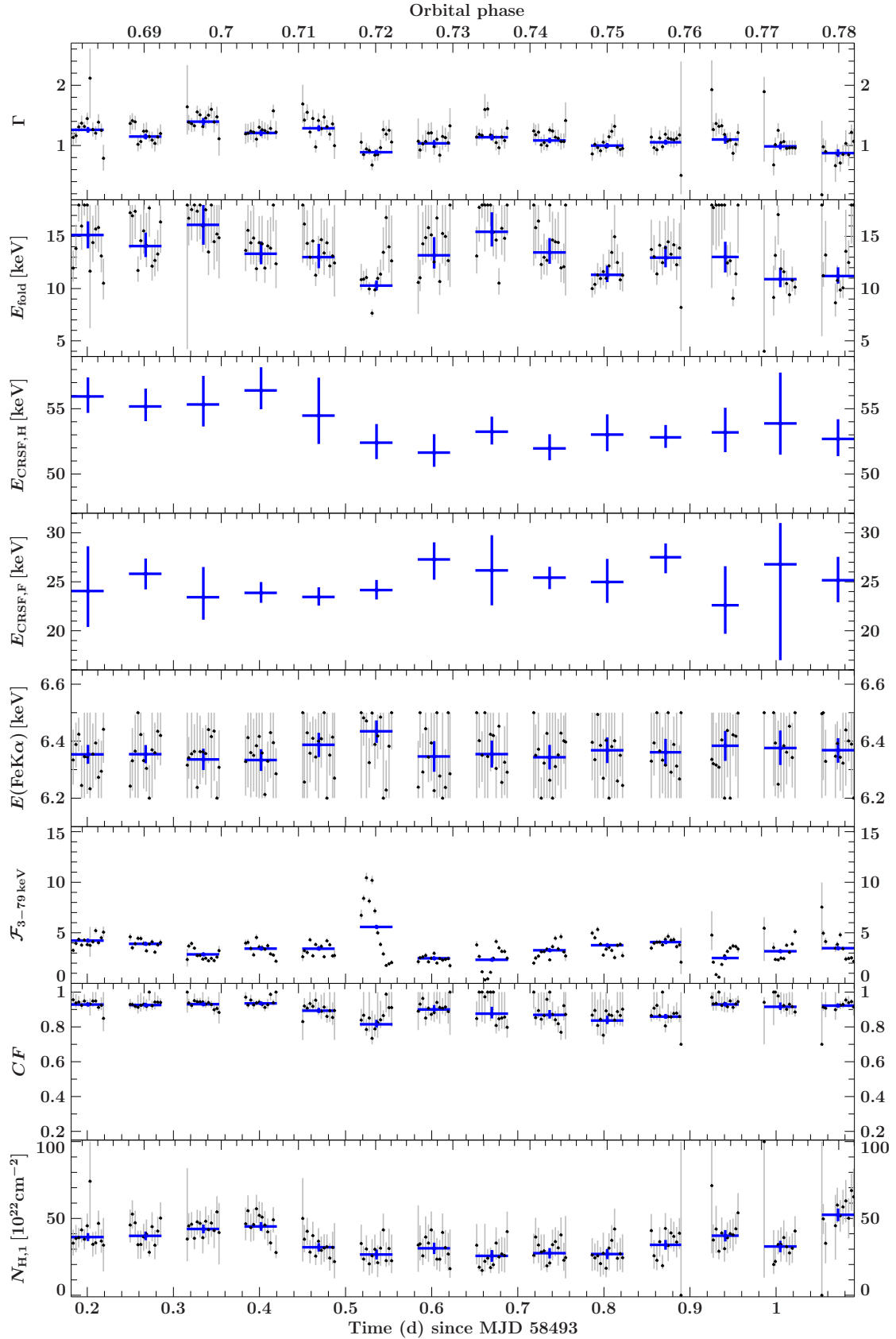


Fig. 6: Results of the pulse-by-pulse (black) and orbit-by-orbit (blue) analyses for observation I as functions of time, showing also the corresponding orbital phase. Top-down description of the panels: photon index Γ , folding energy E_{fold} in keV, energy of the harmonic cyclotron line $E_{\text{CRSF,H}}$ in keV, energy of the fundamental cyclotron line $E_{\text{CRSF,F}}$ in keV, energy of the FeK α line in keV, unabsorbed flux $\mathcal{F}_{3-79 \text{ keV}}$ in $\text{keV s}^{-1} \text{cm}^{-2}$, covering fraction CF, absorption from the stellar wind $N_{\text{H},1}$ in 10^{22}cm^{-2} .

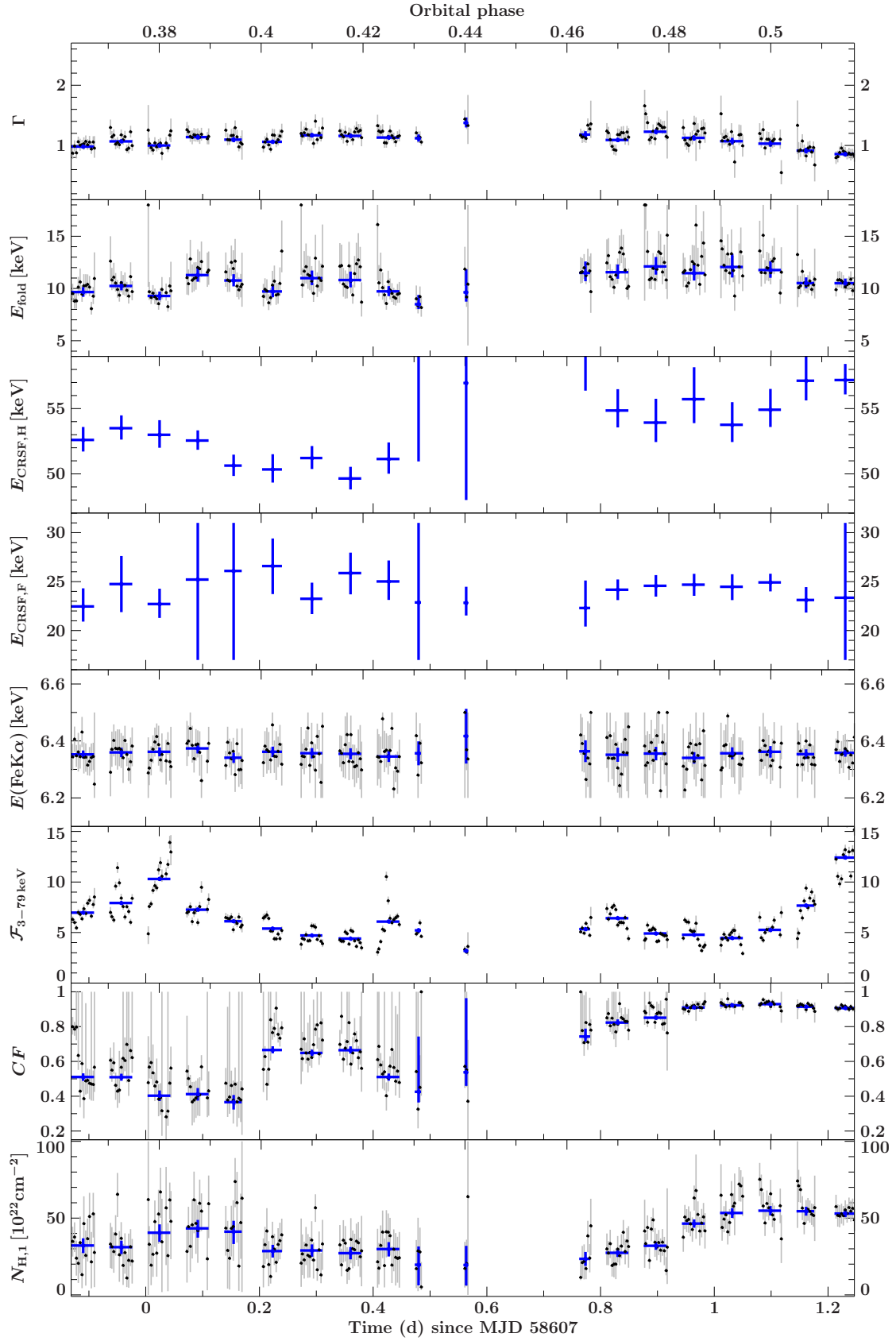


Fig. 7: Results of the pulse-by-pulse (black) and orbit-by-orbit (blue) analyses for observation II as functions of time, showing also the corresponding orbital phase. Top-down description of the panels: photon index Γ , folding energy E_{fold} in keV, energy of the harmonic cyclotron line $E_{\text{CRSF,H}}$ in keV, energy of the fundamental cyclotron line $E_{\text{CRSF,F}}$ in keV, energy of the FeK α line in keV, unabsorbed flux $\mathcal{F}_{3-79 \text{ keV}}$ in $\text{keV s}^{-1} \text{cm}^{-2}$, covering fraction CF , absorption from the stellar wind $N_{\text{H},1}$ in 10^{22}cm^{-2} .

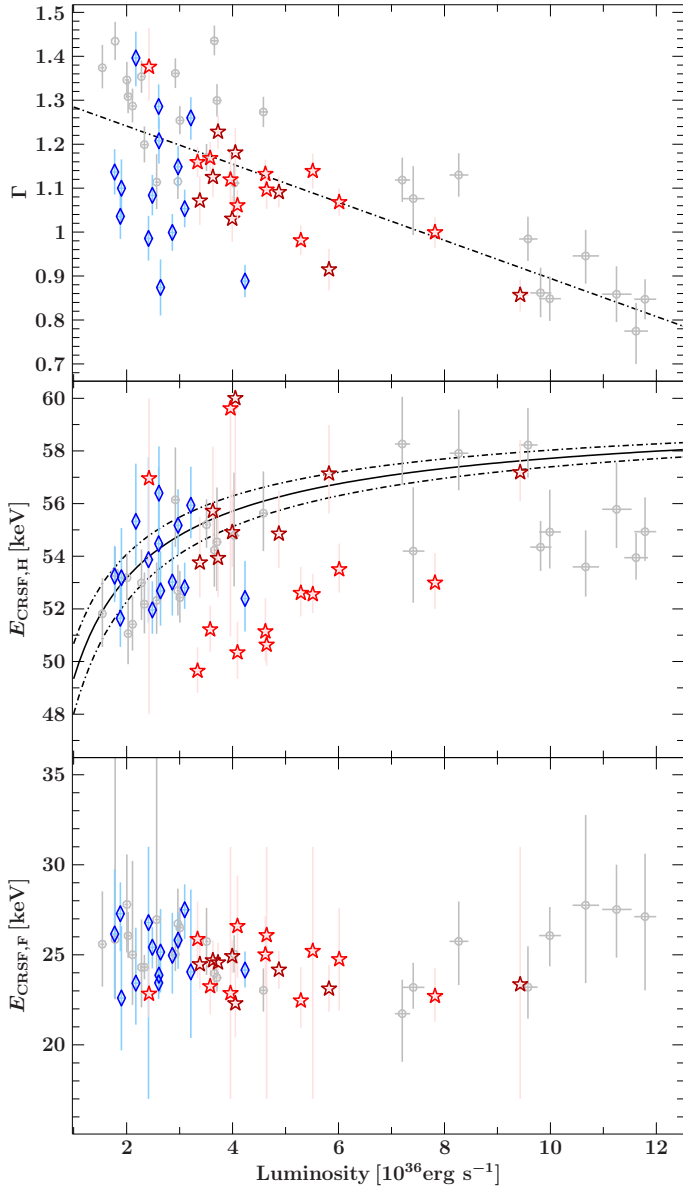


Fig. 8: Spectral parameter as function of the 3–79 keV luminosity based on our orbit-by-orbit spectroscopy results (dark blue diamonds represent observation I, bright red stars observation IIa, and dark red stars observation IIb) together with ks-integrated spectral fits from figure 7 in Fürst et al. (2014b) (grey circles). *Upper panel*: photon index Γ . The black dot-dashed line is a linear regression through all data points, meant to guide the eye. *Middle panel*: energy of the harmonic cyclotron line $E_{\text{CRSF,H}}$. The black solid line is the theoretical prediction for $\Lambda = 1$, $E_{\text{NS}} = 30$ keV and $M_{\text{NS}} = 1.9 M_{\odot}$. The above and below dot-dashed lines are for $M_{\text{NS}} = 1.7 M_{\odot}$ and $M_{\text{NS}} = 2.1 M_{\odot}$ respectively. *Lower panel*: energy of the fundamental line $E_{\text{CRSF,F}}$.

culations assuming $\Lambda = 0.5$. Their critical luminosity for Vela X-1 under these assumptions is of the order of $\sim 0.1\text{--}1 \times 10^{37} \text{ erg s}^{-1}$, which is around our measurements (Fig. 8).

For the Be X-ray binary GRO J1008-57, Kühnel et al. (2017) have computed the theoretically expected critical luminosities at the transition between different accretion regimes after Becker et al. (2012), Mushtukov et al. (2015a), and Postnov et al. (2015) (see their Appendix A). Uncertainties in the theories and data limitations do not allow them to favour one of the theories for the

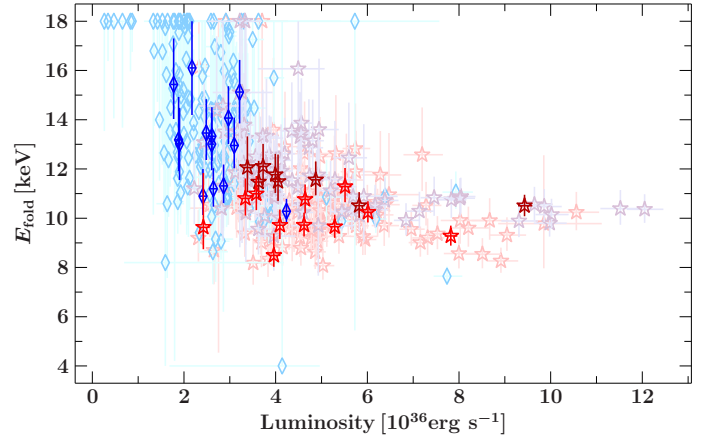


Fig. 9: Folding energy E_{fold} as function of the 3–79 keV luminosity based on our orbit-by-orbit and pulse-by-pulse spectroscopy results. Dark blue diamonds are the results of the orbit-by-orbit analysis for observation I, light blue diamonds are the results of the pulse-by-pulse spectroscopy for observation I, bright red stars are the results of the orbit-by-orbit spectroscopy for observation IIa, pink stars are the results of the pulse-by-pulse spectroscopy for observation IIa, dark red stars are the results of the orbit-by-orbit spectroscopy for observation IIb, lavender stars are the results of the pulse-by-pulse spectroscopy for observation IIb.

prediction of the critical luminosity, similar to our inconclusive results.

Given the above and the fact that neither disc accretion scenario nor the spherical accretion are a good description for the accretion in the highly structured, disturbed wind in the system, estimates on whether Vela X-1 is on sub- or super-critical regime have to be treated with caution. However, for the following section Sect. 6.1.3, we will assume a sub-critical accretion regime for Vela X-1 to compare with previous results.

6.1.3. CRSFs, luminosity, and flares

As we have found a negative correlation between Γ and luminosity for our observations in Sect. 6.1.1, we expect a positive correlation between the cyclotron line energy and the luminosity (see details in Sect. 1) in the case of a sub-critical accretion regime.

The theoretical expected fundamental cyclotron line energy for a sub-critical source can be calculated using equation 7 from Fürst et al. (2014b) with τ_* the Thomson optical depth which we set to 20, the estimate by Becker et al. (2012) for the plasma braking by Coulomb collisions in the filled accretion column and E_{NS} the energy of the fundamental cyclotron energy:

$$E_{\text{theo}} = \left[1 + 0.6 \left(\frac{R_{\text{NS}}}{10 \text{ keV}} \right)^{-\frac{13}{14}} \left(\frac{\Lambda}{0.1} \right)^{-1} \left(\frac{\tau_*}{20} \right) \left(\frac{M_{\text{NS}}}{1.4 M_{\odot}} \right)^{\frac{19}{14}} \right. \\ \left. \times \left(\frac{E_{\text{NS}}}{1 \text{ keV}} \right)^{-\frac{4}{7}} \left(\frac{L_X}{10^{37}} \right)^{-\frac{5}{7}} \right]^{-3} \times E_{\text{NS}} \quad (5)$$

To draw the prediction for the harmonic cyclotron line energy ($n = 2$) and to compare our results with Fürst et al. (2014b), we have to use $2 \times E_{\text{theo}}$. The black dot-dashed line in Fig. 8 top panel shows the expected positive correlation between $E_{\text{CRSF,H}}$ and luminosity in the case of a sub-critical source using $\Lambda = 1$. However, this correlation is hardly visible for our data. This may be

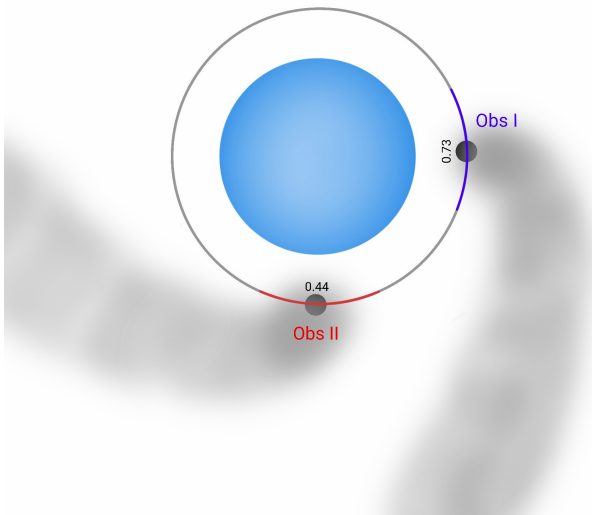


Fig. 10: Sketch of Vela X-1 showing possible positions of the wake structure during the two observations at mid-orbital phase. In this image, the observer’s point of view is located facing the system at the bottom of the picture.

explained by the accretion regime of Vela X-1 lying somewhere in between the sub- and super-critical cases and thus yielding to inconclusive results. Vybornov et al. (2017) also obtained inconclusive results for intermediate accretion regime case for Cep X-4 with collisionless shock theoretical study.

Overall, there seems to be an intrinsic variability in the cyclotron line energies in our observations but they do not appear to be correlated with the luminosity. In particular, in observation I, we observe a clear drop in CRSF energy from ~ 55 – 56 keV to ~ 52 – 53 keV after the flare even though the flux and other spectral parameters return to the pre-flare level (Fig. 6). A similar decrease is seen in observation IIa (Fig. 7), but here the overall flux also decreases. If confirmed, such a behaviour could be explained by re-structuring of the accretion column and thus change in the location of the CRSF producing region following an episode of stronger accretion. To test whether the observed CRSF variability is real, we have re-done the orbit-by-orbit analysis fixing the energies of the cyclotron lines to their respective average value. The overall fit gets worse compared to the analysis with those energies being free and we have not seen changes in the trend observed in other parameters.

6.2. The variable absorption in the stellar wind

6.2.1. Orbital dependency: wakes crossing our line of sight

Because of the structure of the stellar wind, the amount of material being on our line of sight towards the neutron star can change and thus modifies the shape of the continuum creating variability. This is particularly striking with the covering fraction, CF, and the equivalent absorbing hydrogen column density, $N_{H,1}$, showing different behaviours between observations I and II (Figs. 6 and 7) that are taken at different orbital phases when our line of sight crosses different parts of the wind (Fig. 10). The overall structure of the disturbed stellar wind is complex, with both photoionisation and accretion wake present and expected to be variable (Blondin et al. 1990; Malacaria et al. 2016); as our observations cannot distinguish between the components, we refer to them as wakes in general.

Thus, we explore possible correlations between the covering fraction and the column density. Additionally, there are possible modelling degeneracies such as between the slope, Γ , and $N_{H,1}$, inherent to the usage of powerlaw models for the continuum modelling of X-ray binaries (e.g. Suchy et al. 2008). We carefully check for such a correlation both with scatterplots of our orbit-by-orbit and pulse-by-pulse fits (Fig. 11) and through calculation of confidence maps for Γ and $N_{H,1}$ and find that, even if present, it does not significantly contribute to our results.

During observation I, the wakes are located on the line of sight towards the observer. The covering fraction is close to 1, meaning that most of the incoming photons are absorbed through the dense material in the absorption and photoionisation wakes (Blondin et al. 1990; Kaper et al. 1994; Manousakis 2011). This is particularly visible in our time-resolved analysis in Fig. 12 where the orbit-by-orbit and pulse-by-pulse datapoints of observation I show a positive correlation between the stellar wind absorption $N_{H,1}$ and the covering fraction CF. Similar high covering fractions and hydrogen column densities have been seen at this orbital phase in both NuSTAR (Fürst et al. 2014b) and Chandra (Amato et al. 2021) observations.

On the contrary, during observation IIa, the majority of the material in the wakes is not yet on the observer’s line of sight implying a low covering fraction CF and less photons absorbed by the stellar wind (Fig. 10). Indeed, the orbit-by-orbit and pulse-by-pulse datapoints of observation II in Fig. 12 show a negative correlation between the stellar wind absorption $N_{H,1}$ and the covering fraction CF.

Finally, during observation IIb, the wakes are starting to pass through the observer’s line of sight and consequently the CF slowly increases to reach the values of observation I (Fig. 7). This is confirmed by the time-resolved datapoints in Fig. 12 where the same positive correlation than in observation I is seen.

To confirm the physical origin of these behaviours, we calculate the confidence maps for the two parameters of interest, $N_{H,1}$ and CF, using the results from the time-averaged spectroscopy for the three observations, I, IIa and IIb. For observation I, pure modelling degeneracy would lead to a negative correlation between the two parameters, in opposite to what is seen on the scatterplot in Fig. 12, confirming the physical origin to the observed correlation. Similarly, for observation IIa, modelling degeneracy would imply a positive correlation, while the time-resolved datapoints are showing a negative correlation between $N_{H,1}$ and CF also confirming the real event. A possible physical explanation is the overlapping of multiple clumps. The stellar wind surrounding Vela X-1 is clumpy (e.g. Oskinova et al. 2007) and most of the mass of the wind is concentrated in clumps (Sako et al. 1999) so that some of them may be located on our line of sight during an observation. If one clump overlaps with another one, the absorption column density $N_{H,1}$ increases and CF decreases as also observed by Fürst et al. (2014b). For observation IIb, our approach does not detect an explicit modelling degeneracy between $N_{H,1}$ and CF.

6.2.2. Absorption and luminosity

In observations I and IIb, when the wakes are located on the line of sight, Fig. 13 shows that the intrinsic luminosity of the source does not seem to be correlated with the covering fraction CF. Because CF is correlated with $N_{H,1}$ (Fig. 12) for these observations, we do not expect the luminosity of the source to correlate with $N_{H,1}$ either. During a flaring or an off-state period, the fraction of photons absorbed through the stellar wind should be independent from the incoming number of photons if the dense and extended

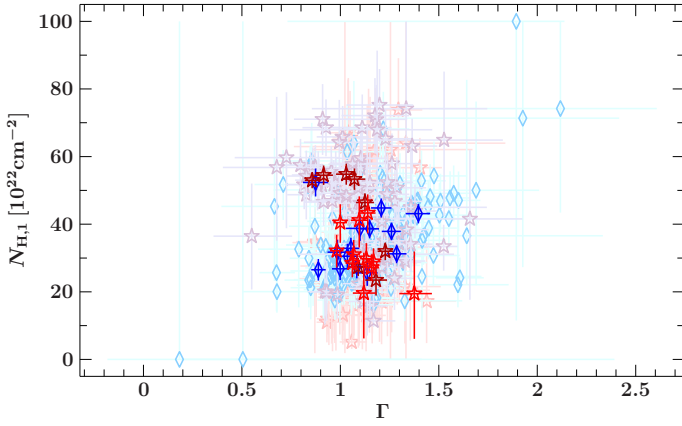


Fig. 11: Stellar wind absorption $N_{H,1}$ as function of the photon index Γ based on our orbit-by-orbit and pulse-by-pulse spectroscopy results. Symbols as in Fig. 9.

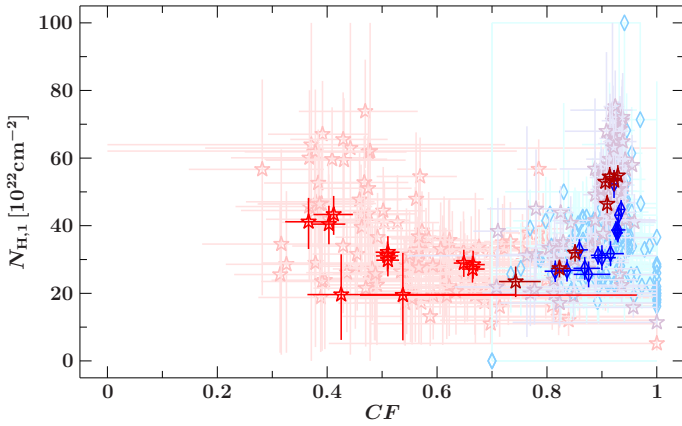


Fig. 12: Stellar wind absorption $N_{H,1}$ as function of the covering fraction CF based on our orbit-by-orbit and pulse-by-pulse spectroscopy results. Symbols as in Fig. 9.

wakes are located on our line of sight as we do not expect them to be strongly influenced by the change in irradiation. However, there are some datapoints of observation I in Fig. 13 with high luminosities ($\sim 6\text{--}8 \times 10^{36} \text{ erg s}^{-1}$) and low CF ($\sim 0.7\text{--}0.8$) that also correspond to a low $N_{H,1}$. They correspond to a decrease of CF and $N_{H,1}$ associated with flares in observations I and IIb (Fig. 6 and 7). This is in agreement with [Odaka et al. \(2013\)](#)⁶ who have found with *Suzaku* observations that the circumstellar absorption does not seem to correlate with the X-ray luminosity except for a strong flare.

[Martínez-Núñez et al. \(2014\)](#) have also observed a decrease in absorption during a giant flare that they attribute to the accretion of a dense clump in the wind. Our observations would support this scenario. Similar changes to the absorbing column density around and during flares have been seen in other wind-accreting sources, including in Supergiant Fast X-ray transients (SFXTs) ([Pradhan et al. 2019](#); [Bozzo et al. 2017](#)).

For observation IIa, the behaviour seems strikingly different (Fig. 13), with possible indications of a negative correlation, although the large uncertainties preclude firm conclusions. Based on our knowledge of the geometry of the system, we interpret

⁶Using the ephemeris listed in Table 2 and employed throughout this paper, the observation discussed in ([Odaka et al. 2013](#)) is at $\phi_{\text{orb}} \approx 0.20\text{--}0.38$.

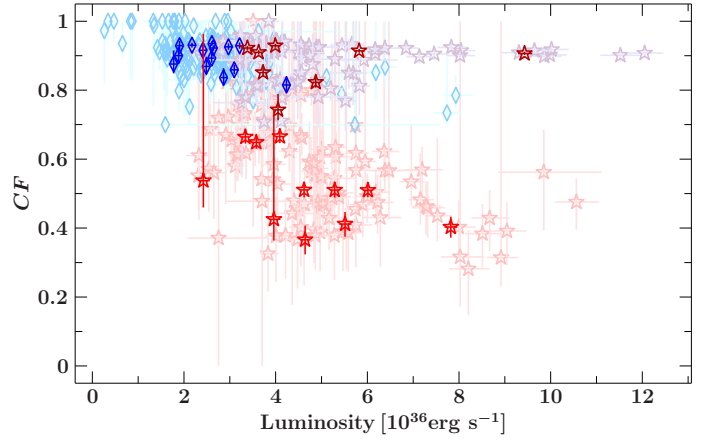


Fig. 13: Covering fraction CF as function of the 3–79 keV luminosity based on our orbit-by-orbit and pulse-by-pulse spectroscopy results. Symbols as in Fig. 9

this as mainly a spurious correlation, linked to events that happen simultaneously in this particular observation by happenstance. At the beginning of observation IIa, the wakes are located outside our line of sight which corresponds to a low covering fraction CF . As seen in Fig. 2, the beginning of observation IIa also coincides with the first flaring period, where a deep local short decrease of CF (see Fig. 7) can also be observed for each flare due to the above described theory of accreted clumps. Similarly, while the wakes are starting to get towards our line of sight, the CF increases and this coincides with a decrease of the X-ray luminosity as the flare subsides (Fig. 2).

The observed energy of the iron line is mostly constant throughout all discussed observations and consistent with neutral iron, except for one notable exception: during the bright flare in observation II, it increases (Fig. 6). This could be indicative of increased ionisation during the flare. Interestingly, however, no increase in the iron line energy is seen in both parts of observation I (Fig. 7) and neither has an increase in the iron line energy been observed in a previous observation of a giant flare by [Martínez-Núñez et al. \(2014\)](#). A careful modelling of our data during the flare does not reveal further possible correlations.

7. Summary and outlook

We analyse two new observations of Vela X-1 taken with *NuSTAR* at different orbital phases and thus probing a different line of sight through the system. For spectral modelling, we use a partial covering model with a powerlaw continuum with a Fermi-Dirac cut-off further modified by CRSFs. We interpret our observations in the context of a highly magnetised neutron star accreting from the clumpy, disturbed wind of a companion and draw conclusions about the accretion geometry and stellar wind structure and their interplay.

Our observations can be explained by denser, extended wakes passing through the line of sight starting at orbital phase of ~ 0.45 . At lower orbital phases, the continuum is less absorbed by the stellar wind. The observed flares and the absorption variability during and around the flaring episodes can be explained by accretion of clumps. It would be interesting, as a future work, to perform a uniform analysis of Vela X-1 at all orbital phases available in order to draw a more complete picture of the stellar wind at different orbital phases ([Kretschmar et al. 2021](#)).

We have confirmed that the photon index is anti-correlated with luminosity, but cannot confirm the suggested correlation of the energy of the harmonic CRSF with flux. While the anti-correlation of the photon index with luminosity points towards sub-critical accretion for Vela X-1, theoretical consideration for the critical luminosity are inconclusive and will require further investigation. The theoretical expectations for the evolution of harmonic CRSF energy with luminosity shown in Fig. 8 are based (unavoidably) on rather simple, mostly fixed geometries. The intermediate case between two accretion regimes for Vela X-1 is the most difficult to treat and it could be interesting in the future to explore more variability than height-scaling in theoretical studies, including full radiation hydro simulations as suggested by Vybornov et al. (2017). Still, we observe variability in CRSF energy and in particular a drop following a flaring episode. Further observations of Vela X-1 and careful analysis of flaring episodes are necessary to test whether this observation was spurious or implies a change in the accretion geometry after a strong flare.

Acknowledgements. We thank the anonymous referee whose input helped to strengthen the paper. This work has been partially funded by the Bundesministerium für Wirtschaft und Energie under the Deutsches Zentrum für Luft- und Raumfahrt Grants 50 OR 1915. SMN acknowledges funding under project RTI2018-096686-B-C21 funded by MCIN/AEI/10.13039/501100011033 and by 'ERDF A way of making Europe', and by the Unidad de Excelencia María de Maeztu, ref. MDM-2017-0765. ESL acknowledges support by DFG grant 1830Wi1860/11-1 and RFBR grant 18-502-12025. KP acknowledges support by NASA under award number 80GSFC17M0002. This work has made use of (1) the Interactive Spectral Interpretation System (ISIS) maintained by Chandra X-ray Center group at MIT; (2) the NuSTAR Data Analysis Software (NuSTARDAS) jointly developed by the ASI Science Data Center (ASDC, Italy) and the California Institute of Technology (Caltech, USA); (3) the of ISIS functions (isisscripts)⁷ provided by ECAP/Remeis observatory and MIT; (4) NASA's Astrophysics Data System Bibliographic Service (ADS). We thank John E. Davis for the development of the `slxfig`⁸ module used to prepare most of the figures in this work.

References

- Amato, R., Grinberg, V., Hell, N., et al. 2021, *A&A*, 648, A105
- Arnaud, K. A. 1996, *Astronomical Society of the Pacific Conference Series*, Vol. 101, XSPEC: The First Ten Years, ed. G. H. Jacoby & J. Barnes, 17
- Basko, M. M. & Sunyaev, R. A. 1976, *MNRAS*, 175, 395
- Becker, P. A., Klochkov, D., Schönherr, G., et al. 2012, *A&A*, 544, A123
- Becker, P. A. & Wolff, M. T. 2007, *ApJ*, 654, 435
- Becker, R. H., Rothschild, R. E., Boldt, E. A., et al. 1978, *ApJ*, 221, 912
- Bildsten, L., Chakrabarty, D., Chiu, J., et al. 1997, *ApJS*, 113, 367
- Bissinger né Kühnel, M., Kreykenbohm, I., Ferrigno, C., et al. 2020, *A&A*, 634, A99
- Blondin, J. M., Kallman, T. R., Fryxell, B. A., & Taam, R. E. 1990, *ApJ*, 356, 591
- Blondin, J. M., Stevens, I. R., & Kallman, T. R. 1991, *ApJ*, 371, 684
- Bozzo, E., Bernardini, F., Ferrigno, C., et al. 2017, *A&A*, 608, A128
- Coburn, W., Heindl, W. A., Rothschild, R. E., et al. 2002, *ApJ*, 580, 394
- de Kool, M. & Anzer, U. 1993, *MNRAS*, 262, 726
- Doroshenko, V., Santangelo, A., Kreykenbohm, I., & Doroshenko, R. 2012, *A&A*, 540, L1
- Doroshenko, V., Santangelo, A., Nakahira, S., et al. 2013, *A&A*, 554, A37
- Doroshenko, V., Santangelo, A., & Suleimanov, V. 2011, *A&A*, 529, A52
- Ducci, L., Sidoli, L., Mereghetti, S., Paizis, A., & Romano, P. 2009, *MNRAS*, 398, 2152
- Eadie, G., Peacock, A., Pounds, K. A., et al. 1975, *MNRAS*, 172, 35P
- El Mellah, I., Sander, A. A. C., Sundqvist, J. O., & Keppens, R. 2019, *A&A*, 622, A189
- El Mellah, I., Sundqvist, J. O., & Keppens, R. 2018, *MNRAS*, 475, 3240
- Ferrigno, C., Becker, P. A., Segreto, A., Mineo, T., & Santangelo, A. 2009, *A&A*, 498, 825
- Fürst, F., Kreykenbohm, I., Pottschmidt, K., et al. 2010, *A&A*, 519, A37
- Fürst, F., Pottschmidt, K., Wilms, J., et al. 2014a, *ApJ*, 784, L40
- Fürst, F., Pottschmidt, K., Wilms, J., et al. 2014b, *ApJ*, 780, 133
- Goldstein, G., Huenemoerder, D. P., & Blank, D. 2004, *AJ*, 127, 2310
- Grinberg, V., Hell, N., El Mellah, I., et al. 2017, *A&A*, 608, A143
- Haberl, F. & White, N. E. 1990, *ApJ*, 361, 225
- Harrison, F. A., Craig, W. W., Christensen, F. E., et al. 2013, *ApJ*, 770, 103
- Hemphill, P. B., Rothschild, R. E., Markowitz, A., et al. 2014, *ApJ*, 792, 14
- H14PT Collaboration, Ben Bekhti, N., Flöer, L., et al. 2016, *A&A*, 594, A116
- Hiltner, W. A., Werner, J., & Osmer, P. 1972, *ApJ*, 175, L19
- Houck, J. C. & Denicola, L. A. 2000, *Astronomical Society of the Pacific Conference Series*, Vol. 216, ISIS: An Interactive Spectral Interpretation System for High Resolution X-Ray Spectroscopy, ed. N. Manset, C. Veillet, & D. Crabtree, 591
- Jaisawal, G. K. & Naik, S. 2016, *MNRAS*, 461, L97
- Kaper, L., Hammerslag-Hensberge, G., & Zuiderwijk, E. J. 1994, *A&A*, 289, 846
- Kendziorra, E., Mony, B., Kretschmar, P., et al. 1992, in *Frontiers Science Series*, ed. Y. Tanaka & K. Koyama, 51
- Klochkov, D., Horns, D., Santangelo, A., et al. 2007, *A&A*, 464, L45
- Klochkov, D., Stauber, R., Santangelo, A., Rothschild, R. E., & Ferrigno, C. 2011, *A&A*, 532, A126
- Kretschmar, P., El Mellah, I., Martínez-Núñez, S., et al. 2021, *A&A*, 652, A95
- Kretschmar, P., Pan, H. C., Kendziorra, E., et al. 1997, *A&A*, 325, 623
- Kreykenbohm, I., Coburn, W., Wilms, J., et al. 2002, *A&A*, 395, 129
- Kreykenbohm, I., Kretschmar, P., Wilms, J., et al. 1999, *A&A*, 341, 141
- Kreykenbohm, I., Wilms, J., Kretschmar, P., et al. 2008, *A&A*, 492, 511
- Kühnel, M., Fürst, F., Pottschmidt, K., et al. 2017, *A&A*, 607, A88
- La Barbera, A., Santangelo, A., Orlandini, M., & Segreto, A. 2003, *A&A*, 400, 993
- Lamb, F. K., Pethick, C. J., & Pines, D. 1973, *ApJ*, 184, 271
- Langer, S. H. & Rappaport, S. 1982, *ApJ*, 257, 733
- Larsen, A. N. & Monakhov, E. V. 1996, *Nuclear Instruments and Methods in Physics Research B*, 117, 71
- Leahy, D. A. 1987, *A&A*, 180, 275
- Legred, I., Chatziioannou, K., Essick, R., Han, S., & Landry, P. 2021, *arXiv e-prints*, arXiv:2106.05313
- Liao, Z., Liu, J., Zheng, X., & Gou, L. 2020, *MNRAS*, 492, 5922
- Lomaeva, M., Grinberg, V., Guainazzi, M., et al. 2020, *A&A*, 641, A144
- Madsen, K. K., Grefenstette, B. W., Pike, S., et al. 2020, *arXiv e-prints*, arXiv:2005.00569
- Maitra, C. & Paul, B. 2013, *ApJ*, 763, 79
- Makishima, K., Mihara, T., Nagase, F., & Tanaka, Y. 1999, *ApJ*, 525, 978
- Malacaria, C., Mihara, T., Santangelo, A., et al. 2016, *A&A*, 588, A100
- Manousakis, A. 2011, PhD thesis, Université de Genève
- Manousakis, A. & Walter, R. 2015, *A&A*, 575, A58
- Martínez-Núñez, S., Torrejón, J. M., Kühnel, M., et al. 2014, *A&A*, 563, A70
- McBride, V. A., Wilms, J., Coe, M. J., et al. 2006, *A&A*, 451, 267
- McClintock, J. E., Rappaport, S., Joss, P. C., et al. 1976, *ApJ*, 206, L99
- Mihara, T. 1995, PhD thesis, -
- Müller, S., Ferrigno, C., Kühnel, M., et al. 2013, *A&A*, 551, A6
- Mushtukov, A. A., Suleimanov, V. F., Tsygankov, S. S., & Poutanen, J. 2015a, *MNRAS*, 447, 1847
- Mushtukov, A. A., Tsygankov, S. S., Serber, A. V., Suleimanov, V. F., & Poutanen, J. 2015b, *MNRAS*, 454, 2714
- Nagase, F., Hayakawa, S., Makino, F., Sato, N., & Makishima, K. 1983, *PASJ*, 35, 47
- Nespoli, E., Reig, P., & Zezas, A. 2012, *A&A*, 547, A103
- Nishimura, O. 2014, *ApJ*, 781, 30
- Odaka, H., Khangulyan, D., Tanaka, Y. T., et al. 2013, *ApJ*, 767, 70
- Orlandini, M., Dal Fiume, D., Frontera, F., et al. 1998, *A&A*, 332, 121
- Oskinova, L. M., Hamann, W. R., & Feldmeier, A. 2007, *A&A*, 476, 1331
- Postnov, K. A., Gornostaev, M. I., Klochkov, D., et al. 2015, *MNRAS*, 452, 1601
- Poutanen, J., Mushtukov, A. A., Suleimanov, V. F., et al. 2013, *ApJ*, 777, 115
- Pradhan, P., Bozzo, E., Paul, B., Manousakis, A., & Ferrigno, C. 2019, *ApJ*, 883, 116
- Quaintrell, H., Norton, A. J., Ash, T. D. C., et al. 2003, *A&A*, 401, 313
- Reig, P. & Milonaki, F. 2016, *A&A*, 594, A45
- Reig, P. & Nespoli, E. 2013, *A&A*, 551, A1
- Rothschild, R. E., Kühnel, M., Pottschmidt, K., et al. 2017, *MNRAS*, 466, 2752
- Sako, M., Liedahl, D. A., Kahn, S. M., & Paerels, F. 1999, *ApJ*, 525, 921
- Santangelo, A., del Sordo, S., Segreto, A., et al. 1998, *A&A*, 340, L55
- Sato, N., Hayakawa, S., Nagase, F., et al. 1986, *PASJ*, 38, 731
- Schwarm, F. W., Schönherr, G., Falkner, S., et al. 2017, *A&A*, 597, A3
- Shapiro, S. L. & Salpeter, E. E. 1975, *ApJ*, 198, 671
- Sidoli, L., Paizis, A., Fürst, F., et al. 2015, *MNRAS*, 447, 1299
- Stauber, R., Shakura, N. I., Postnov, K., et al. 2007, *A&A*, 465, L25
- Stauber, R., Trümper, J., Kendziorra, E., et al. 2019, *A&A*, 622, A61
- Suchy, S., Pottschmidt, K., Wilms, J., et al. 2008, *ApJ*, 675, 1487
- Tanaka, Y. 1986, in *Proc. IAU Colloq.* 89, Vol. 255, *Radiation Hydrodynamics in Stars and Compact Objects*, ed. D. Mihalas & K.-H. A. Winkler (Springer-Verlag New York)
- Titarchuk, L. 1994, *ApJ*, 434, 570
- Tsygankov, S. S., Rouco Escorial, A., Suleimanov, V. F., et al. 2019, *MNRAS*, 483, L144
- van Kerkwijk, M. H., van Paradijs, J., & Zuiderwijk, E. J. 1995, *A&A*, 303, 497
- van Loon, J. T., Kaper, L., & Hammerslag-Hensberge, G. 2001, *A&A*, 375, 498
- Verner, D. A., Ferland, G. J., Korista, K. T., & Yakovlev, D. G. 1996, *ApJ*, 465, 487
- Vybornov, V., Klochkov, D., Gornostaev, M., et al. 2017, *A&A*, 601, A126
- Watanabe, S., Sako, M., Ishida, M., et al. 2006, *ApJ*, 651, 421
- Wilms, J., Allen, A., & McCray, R. 2000, *ApJ*, 542, 914
- Yamamoto, T., Sugizaki, M., Mihara, T., et al. 2011, *Publications of The Astronomical Society of Japan - PUBL ASTRON SOC JPN*, 63

⁷<http://www.sternwarte.uni-erlangen.de/isis/>

⁸<http://www.jedsoft.org/fun/slxfig/>

Appendix A: Appendix

Table A.1: Best-fit parameters for the time-averaged tested models for observation I.

Parameter	FDcut	FDcut (w/o 10 keV)	highcut (w/o 10 keV)	
C_{FPMA}	1	1	1	1
C_{FPMB}	1.0203 ± 0.0021	1.0203 ± 0.0021	1.0203 ± 0.0021	1.0204 ± 0.0021
$N_{\text{H},1} (10^{22} \text{ cm}^{-2})$	34.0 ± 1.0	34.4 ± 1.0	$36.4^{+1.0}_{-1.1}$	$35.2^{+0.9}_{-1.0}$
$N_{\text{H},2} (10^{22} \text{ cm}^{-2})$	fixed to 0.371	fixed to 0.371	fixed to 0.371	fixed to 0.371
Γ	1.09 ± 0.05	$1.294^{+0.017}_{-0.033}$	$1.373^{+0.015}_{-0.017}$	1.353 ± 0.016
$E_{\text{cut}} (\text{keV})$	$19.9^{+3.5}_{-2.0}$	40^{+0}_{-5}	$25.6^{+0.5}_{-0.4}$	$28.1^{+0.7}_{-1.0}$
$E_{\text{fold}} (\text{keV})$	$12.6^{+0.9}_{-0.8}$	$10.5^{+1.0}_{-0.7}$	$15.0^{+0.7}_{-0.6}$	$16.0^{+1.2}_{-1.0}$
$E_{\text{CRSF,F}} (\text{keV})$	$24.7^{+1.0}_{-0.9}$	$27.38^{+0.26}_{-0.29}$	$25.8^{+0.9}_{-0.4}$	$27.6^{+0.5}_{-0.6}$
$\sigma_{\text{CRSF,F}} (\text{keV})$	$0.5 \times \sigma_{\text{CRSF,H}}$	$0.5 \times \sigma_{\text{CRSF,H}}$	$0.5 \times \sigma_{\text{CRSF,H}}$	$0.5 \times \sigma_{\text{CRSF,H}}$
$d_{\text{CRSF,F}} (\text{keV})$	$0.75^{+0.00}_{-0.19}$	$2.82^{+0.15}_{-0.61}$	3.3 ± 0.4	$4.9^{+0.4}_{-0.5}$
$E_{\text{CRSF,H}} (\text{keV})$	$53.8^{+1.1}_{-0.9}$	53.6 ± 0.8	54.4 ± 0.5	55.3 ± 0.7
$\sigma_{\text{CRSF,H}} (\text{keV})$	$7.9^{+1.3}_{-0.9}$	$10.9^{+0.4}_{-0.8}$	$8.7^{+2.0}_{-0.6}$	$10.7^{+0.5}_{-0.7}$
$d_{\text{CRSF,H}} (\text{keV})$	18^{+6}_{-4}	38^{+4}_{-9}	$19.4^{+14.0}_{-2.9}$	33 ± 6
$E_{\text{FeK}\alpha} (\text{keV})$	6.364 ± 0.012	6.365 ± 0.012	6.365 ± 0.012	6.367 ± 0.012
$A_{\text{FeK}\alpha} (\text{ph s}^{-1} \text{ cm}^{-2})$	$(1.35 \pm 0.11) \times 10^{-3}$	$(1.44 \pm 0.11) \times 10^{-3}$	$(1.39^{+0.13}_{-0.11}) \times 10^{-3}$	$(1.36 \pm 0.11) \times 10^{-3}$
$\sigma_{\text{FeK}\alpha} (\text{keV})$	$0.070^{+0.029}_{-0.045}$	$0.084^{+0.027}_{-0.033}$	$0.07^{+0.04}_{-0.05}$	$0.067^{+0.029}_{-0.053}$
$E_{10 \text{ keV}} (\text{keV})$	$9.5^{+0.6}_{-1.0}$	—	$8.00^{+0.27}_{-0.00}$	—
$A_{10 \text{ keV}} (\text{ph s}^{-1} \text{ cm}^{-2})$	$(-4.8^{+2.2}_{-4.8}) \times 10^{-3}$	—	$(4.8^{+2.1}_{-1.1}) \times 10^{-4}$	—
$\sigma_{10 \text{ keV}} (\text{keV})$	$3.2^{+1.0}_{-0.7}$	—	$0.40^{+0.32}_{-0.11}$	—
$\mathcal{F}_{3-79 \text{ keV}} (\text{keV s}^{-1} \text{ cm}^{-2})$	$3.43^{+0.10}_{-0.05}$	$3.91^{+0.05}_{-0.21}$	$3.642^{+0.012}_{-0.053}$	$3.92^{+0.10}_{-0.11}$
CF	0.883 ± 0.005	0.898 ± 0.004	$0.8979^{+0.0031}_{-0.0030}$	0.901 ± 0.004
χ^2/dof	613.37/456	692.60/459	617.16/456	698.07/459

Table A.2: Best-fit parameters for the time-averaged tested models for observation I.

Parameter	single compTT	single compTT (w/o 10 keV)	double compTT	NPEX (w/o 10 keV)	1
C_{FPMA}	1	1	1	1	1
C_{FPMB}	1.0203 ± 0.0021	1.0203 ± 0.0021	1.0203 ± 0.0021	1.0203 ± 0.0021	1.0203 ± 0.0021
$N_{\text{H},1}$ (10^{22} cm^{-2})	$37.0^{+1.3}_{-1.4}$	35.8 ± 1.1	35.5 ± 1.2	34.3 ± 1.1	34.3 ± 1.0
$N_{\text{H},2}$ (10^{22} cm^{-2})	fixed to 0.371	fixed to 0.371	fixed to 0.371	fixed to 0.371	fixed to 0.371
Γ_1	–	–	–	-0.51 ± 0.14	-0.71 ± 0.04
$\Gamma_{1,\text{norm}}$	–	–	–	$0.164^{+0.039}_{-0.030}$	0.167 ± 0.010
Γ_2	–	–	–	fixed to 2	fixed to 2
$\Gamma_{2,\text{norm}}$	–	–	–	$(1.3^{+0.6}_{-0.5}) \times 10^{-3}$	$(1.07^{+0.11}_{-0.10}) \times 10^{-4}$
E_{cut} (keV)	–	–	–	$6.33^{+0.38}_{-0.29}$	$7.75^{+0.34}_{-0.30}$
$\text{compTT}_{\text{norm},1}$	$0.0559^{+0.0032}_{-0.0028}$	$0.0541^{+0.0024}_{-0.0023}$	$0.052^{+0.009}_{-0.025}$	–	–
$T_{0,1}$ (keV)	$0.94^{+0.05}_{-0.07}$	$1.000^{+0.000}_{-0.008}$	$1.000^{+0.000}_{-0.018}$	–	–
kT_1 (keV)	$8.3^{+0.5}_{-0.4}$	8.2 ± 0.5	$6.9^{+0.4}_{-0.8}$	–	–
τ_1	10.43 ± 0.22	$10.52^{+0.23}_{-0.22}$	$11.9^{+1.2}_{-0.9}$	–	–
$\text{compTT}_{\text{norm},2}$	–	–	$(6^{+25}_{-5}) \times 10^{-3}$	–	–
$T_{0,2}$ (keV)	–	–	fixed to $T_{0,1}$	–	–
kT_2 (keV)	–	–	$12.3^{+2.7}_{-4.2}$	–	–
τ_2	–	–	$6.6^{+6.3}_{-1.6}$	–	–
$E_{\text{CRSF},F}$ (keV)	$26.29^{+0.31}_{-0.00}$	26.2 ± 0.4	$24.9^{+0.8}_{-0.6}$	27.9 ± 0.7	26.62 ± 0.29
$\sigma_{\text{CRSF},F}$ (keV)	$0.5 \times \sigma_{\text{CRSF},H}$	$0.5 \times \sigma_{\text{CRSF},H}$	$0.5 \times \sigma_{\text{CRSF},H}$	$0.5 \times \sigma_{\text{CRSF},H}$	$0.5 \times \sigma_{\text{CRSF},H}$
$d_{\text{CRSF},F}$ (keV)	2.7 ± 0.7	2.7 ± 0.8	$0.85^{+0.44}_{-0.20}$	$18.7^{+2.4}_{-3.9}$	$3.6^{+0.8}_{-0.7}$
$E_{\text{CRSF},H}$ (keV)	54.9 ± 0.9	54.9 ± 1.0	$53.6^{+1.0}_{-0.8}$	$51.7^{+1.2}_{-1.0}$	54.5 ± 0.8
$\sigma_{\text{CRSF},H}$ (keV)	$11.0^{+0.9}_{-1.0}$	$11.0^{+1.0}_{-1.1}$	$7.6^{+1.3}_{-0.8}$	$14.2^{+0.9}_{-0.0}$	11.5 ± 0.8
$d_{\text{CRSF},H}$ (keV)	36^{+10}_{-9}	35^{+11}_{-10}	$16.2^{+3.9}_{-3.0}$	83 ± 10	40^{+10}_{-8}
$E_{\text{Fe}\alpha}$ (keV)	6.368 ± 0.012	6.368 ± 0.012	6.368 ± 0.012	6.364 ± 0.012	6.365 ± 0.012
$A_{\text{Fe}\alpha}$ ($\text{ph s}^{-1} \text{ cm}^{-2}$)	$(1.44^{+0.12}_{-0.11}) \times 10^{-3}$	$(1.37 \pm 0.11) \times 10^{-3}$	$(1.40 \pm 0.11) \times 10^{-3}$	$(1.36 \pm 0.11) \times 10^{-3}$	$(1.40 \pm 0.11) \times 10^{-3}$
$\sigma_{\text{Fe}\alpha}$ (keV)	$0.084^{+0.027}_{-0.034}$	$0.076^{+0.028}_{-0.037}$	$0.082^{+0.027}_{-0.035}$	$0.072^{+0.029}_{-0.042}$	$0.078^{+0.028}_{-0.037}$
$E_{10 \text{ keV}}$ (keV)	$8.39^{+0.26}_{-0.20}$	–	–	$9.8^{+0.5}_{-0.8}$	–
$A_{10 \text{ keV}}$ ($\text{ph s}^{-1} \text{ cm}^{-2}$)	$(5.3^{+3.1}_{-2.4}) \times 10^{-4}$	–	–	-0.37 ± 0.11	–
$\sigma_{10 \text{ keV}}$ (keV)	$0.71^{+0.23}_{-0.20}$	–	–	$6.6^{+0.5}_{-0.4}$	–
CF	$0.842^{+0.014}_{-0.012}$	$0.831^{+0.005}_{-0.004}$	0.830 ± 0.005	0.878 ± 0.010	0.882 ± 0.005
χ^2/dof	$604.45/456$	$630.30/459$	$622.53/456$	$604.15/456$	$644.55/459$